The Fundamental Plane of cluster spheroidal galaxies at $z \sim 1.3$: evidence for mass-dependent evolution

P. Saracco [1]⋆ A. Gargiulo,[2] F. La Barbera [3] M. Annunziatella[4] and D. Marchesini[4]

[1]*INAF – Osservatorio Astronomico di Brera, via Brera 28, I-20121 Milano, Italy*
[2]*INAF – Istituto di Astrofisica e Fisica Cosmica, IASF, via A. Corti 12, I-20133 Milano, Italy*
[3]*INAF – Osservatorio Astronomico di Capodimonte, sal. Moiariello 16, I-80131 Napoli, Italy*
[4]*Physics and Astronomy Department, Tufts University, 574 Boston Ave, Medford, I-02155 MA, USA*

ABSTRACT

We present spectroscopic observations obtained at the Large Binocular Telescope in the field of the cluster XLSSJ0223−0436 at $z = 1.22$. We confirm 12 spheroids cluster members and determine stellar velocity dispersion for 7 of them. We combine these data with those in the literature for clusters RXJ0848+4453 at $z = 1.27$ (8 galaxies) and XMMJ2235−2557 at $z = 1.39$ (7 galaxies) to determine the Fundamental Plane (FP) of cluster spheroids. We find that the FP at $z \sim 1.3$ is offset and rotated ($\sim 3\sigma$) with respect to the local FP. The offset corresponds to a mean evolution $\Delta\log(M_{\rm dyn}/L_{\rm B}) = (-0.5 \pm 0.1)z$. High-redshift galaxies follow a steeper mass-dependent $M_{\rm dyn}/L_{\rm B}$–$M_{\rm dyn}$ relation than local ones. Assuming $\Delta\log(M_{\rm dyn}/L_{\rm B}) = \Delta\log(M^*/L_{\rm B})$, higher mass galaxies [$\log(M_{\rm dyn}/M_\odot) \geq 11.5$] have a higher formation redshift ($z_{\rm f} \geq 6.5$) than lower mass ones [$z_{\rm f} \leq 2$ for $\log(M_{\rm dyn}/M_\odot \leq 10)$], with a median $z_{\rm f} \simeq 2.5$ for the whole sample. Also, galaxies with higher stellar mass density host stellar populations formed earlier than those in lower density galaxies. At fixed initial mass function, $M_{\rm dyn}/M^*$ varies systematically with mass and mass density. It follows that the evolution of the stellar populations ($M^*/L_{\rm B}$) accounts for the observed evolution of $M_{\rm dyn}/L_{\rm B}$ for $M_{\rm dyn} > 10^{11}$ $M_\odot$ galaxies, while accounts for ~ 85 per cent of the evolution at $M_{\rm dyn} < 10^{11}$ $M_\odot$. We find no evidence in favour of structural evolution of individual galaxies, while we find evidences that spheroids later added to the population may account for the observed discrepancy between $\Delta\log(M_{\rm dyn}/L_{\rm B})$ and $\Delta\log(M^*/L_{\rm B})$ at masses $<10^{11}$ $M_\odot$. Thus, the evolution of the FP of cluster spheroids is consistent with the mass-dependent and mass density-dependent evolution of their stellar populations superimposed to a minor contribution of spheroids joining the population at later times.

Key words: galaxies: elliptical and lenticular, cD – galaxies: evolution – galaxies: formation – galaxies: high-redshift.

1 INTRODUCTION

The process of stellar mass growth in galaxies has led to lock more than 60 per cent of stars in the local Universe in spheroidal galaxies (e.g. Fukugita, Hogan & Peebles 1998). The recent deep and wide multiwavelength surveys have shown that massive ($M^* > 10^{11}$ $M_\odot$) spheroids were already present in the first 2 Gyr of cosmic time ($z > 3$; e.g. Glazebrook et al. 2017) and that they were characterized by an old stellar population when compared to the age of the Universe at that redshift (e.g. Kriek et al. 2016). The mechanisms through which spheroids assembled and shaped their stellar mass, quenched their star formation and evolved along the cosmic time are still unclear and represent challenging problems in modern astrophysics.

To reproduce the properties of spheroidal galaxies and to match the observed tight scaling relations, simulations suggest that an early intense burst of star formation followed by a quick quenching are required (Ciotti, Lanzoni & Volonteri 2007; Naab et al. 2007; Oser et al. 2012; Porter et al. 2014; Brooks & Christensen 2016). Observations of local spheroids show that a minor fraction of spheroids may accrete newly stellar mass through secondary events of star formation (e.g. Thomas et al. 2010). Therefore, studying spheroidal galaxies at high-redshift provides stringent information of the main episode of their stellar mass growth.

Environment seems to promote some mechanisms with respect to others, affecting the morphological mix of the galaxies but not their properties. For instance, the spheroidal galaxy fraction reaches even 70–80 per cent in the core of some clusters, twice the one observed

in the field (e.g. Dressler 1980; Holden et al. 2007; van der Wel et al. 2007). There seems to be a lack of massive ($M^* > 2 \times 10^{11}$ $M_\odot$) and hence large ($R_e > 4$–5 kpc) spheroids in the field with respect to cluster (e.g. Saracco et al. 2017), even if they do not differ from each other at fixed stellar mass (e.g. Huertas-Company et al. 2013b; Newman et al. 2014; Kelkar et al. 2015; Saracco et al. 2017). Thus, observations of cluster environment represent an efficient way to collect representative samples of spheroidal galaxies to study.

Some studies based on the Fundamental Plane (FP) of spheroidal galaxies at intermediate redshift (up to $z \sim 0.9$) show that their evolution is consistent with a simple aging of their stellar populations (e.g. Jørgensen et al. 2006; van Dokkum & van der Marel 2007). Other studies suggest that a structural evolution of individual galaxies (a variation of R_e and σ_e) besides their simple aging is required to account for the FP evolution (e.g. Saglia et al. 2010, 2016; Beifiori et al. 2017) even if progenitor bias could affect significantly this interpretation (Prichard et al. 2017). Moreover, while some authors find a steepening of the FP slope with redshift (di Serego Alighieri et al. 2005; Jørgensen et al. 2006; Jørgensen & Chiboucas 2013), other authors do not detect any variation (e.g. Holden et al. 2010).

A steeper FP at higher redshift could be explained in terms of a mass-dependent evolution of galaxies, with higher mass galaxies forming their stars at higher redshifts than lower mass ones. Also other properties may cause a differential evolution of galaxies and hence of the FP. For instance, stellar metallicity and, at a less extent, age are found to correlate with velocity dispersion and dynamical mass in local (e.g. Jørgensen 1999; Trager et al. 2000; Gallazzi et al. 2005, 2014; Thomas et al. 2005, 2010; Harrison et al. 2011; McDermid et al. 2015) and high-redshift spheroids (e.g. Jørgensen et al. 2017; Saracco et al. 2019). These correlations imply a mass-dependent evolution of the luminosity of galaxies and, consequently, a variation of the FP slope. Stellar metallicity is also correlated with the stellar mass density (e.g. Saracco et al. 2019), and stellar population properties are found to correlate with some structural properties of galaxies (e.g. Zahid & Geller 2017; van de Sande et al. 2018).

Whether the FP slope changes along cosmic time is still a matter of debate. Analogously, whether and how the above relationships affect the FP and its evolution is not well understood. In this paper, we try to address these issues starting from the determination of the FP of cluster spheroids at $z \sim 1.3$ and establishing its evolution. To this end, we have obtained new spectroscopic observations of candidate members of the cluster XLSSJ0223−0436 at $z \sim 1.22$ deriving stellar velocity dispersion for seven spheroids cluster members. Combining these data with those in the literature for the clusters RXJ0848+4453 at $z = 1.27$ (eight galaxies; Jørgensen et al. 2014) and XMMJ2235−2557 at $z = 1.39$ (seven galaxies; Beifiori et al. 2017), we constructed an homogeneous and unbiased sample of 22 cluster spheroids to determine, for the first time, the FP at ~ 1.3 and its evolution both in term of offset and slope over the last 9 Gyr.

The paper is organized as follows. Section 2 describes the observations, the data reduction, and the redshift measurement. Section 3 describes the velocity dispersion measurement and the dynamical mass derivation. Section 4 describes the high redshift and the local reference samples used to derive the FP at ~ 1.3 and in the local Universe. In Section 5, the evolution of the M_{dyn}/L_B is derived and used to constrain the formation redshift of cluster spheroids. Section 6 discusses the evolution that spheroids likely experience since $z \sim 1.3$ that account for the FP evolution derived

in the previous sections. Section 7 presents a summary of results and the conclusions.

Throughout this paper, we use a cosmology with $H_0 = 70$ Km s^{-1} Mpc^{-1}, $\Omega_m = 0.3$ and $\Omega_\Lambda = 0.7$, and assume a Chabrier (Chabrier 2003) initial stellar mass function. All the magnitudes are in the Vega system, unless otherwise specified.

2 OBSERVATIONS, DATA REDUCTION, AND REDSHIFT MEASUREMENT

2.1 Spectroscopic observations and data reduction

Spectroscopic observations in the field of the cluster XLSSJ0223−0436 at $z = 1.22$ were performed with the Multi-Object Double Spectrograph (MODS, 1 and 2; Pogge et al. 2010) mounted at the Large Binocular Telescope (LBT). Filter GG495 coupled with the grim G670L sampling the wavelength range $0.5 < \lambda < 1.0$ μm at 0.85 Å pixel^{-1} and a slit width of 1.2 arcsec were adopted. The resulting spectral resolution is $R \simeq 1150$ (FWHM $\simeq 7.4$ Å). The 22 targeted galaxies within 1 arcmin radius from the cluster centre were arranged into two masks and are listed in Table 1. The selection of the parent sample of spheroids cluster member candidates from which the main targets were selected is described in Saracco et al. (2017) and Saracco et al. (2019).

Observations for each mask were collected with MODS1 and MODS2 cameras from 2015 October to 2016 January. The seeing was in the range FWHM = 0.7–1.1 arcsec. Observations consisted in a sequence of exposures of 900 s each taken at dithered (ABBA) positions offset by ∼5 arcsec. A total of 32 and 35 exposures were collected for the two masks, respectively, summing up to an effective integration time of about 8 h. The same bright star was included in the two masks in order to accurately measure the offsets in the observing sequence and the correction for telluric absorption lines. A detailed description of the observations and of the data reduction is given in Saracco et al. (2019).

The spectra thus obtained were used to derive redshifts and for the seven main targets having sufficient signal-to-noise ratio (S/N) and velocity dispersion.

2.2 Redshift measurement

Redshift and velocity dispersion measurements were performed by fitting the observed spectra with MILES simple stellar population (SSP) models (Vazdekis et al. 2010) having a spectral resolution of 2.5 Å (Beifiori et al. 2011), higher than the rest-frame resolution (∼3.3 Å) of our spectra. The spectral fitting was performed using the penalized PiXel-Fitting (PPXF) method (Cappellari & Emsellem 2004; Cappellari 2017).

We derived redshifts for 21 out of the 22 target galaxies. In Table 1, we report the values of the estimated redshifts. We considered secure the redshifts for those galaxies (18) clearly showing one or more spectral (absorption and/or emission) features and/or the 4000 Å break, while we considered insecure the redshifts derived only from the fitting to the overall shape of the continuum with no clear features. In these latter cases (galaxies #474, #962, and #1320), the values are shown in brackets in Table 1. Out of the 21 galaxies with redshift measurements, 12 spheroidal galaxies are confirmed members of the cluster. For seven of them, the S/N measured in the wavelength range 3900–4100 Å, turned out to be sufficient (S/N ∼ 3–8 per Å, 6–18 in the rest frame) to derive stellar velocity dispersion. Fig. 1 shows the spectra of the seven spheroidal galaxies with higher S/N, while Fig. 1 shows the spectra of the

Table 1. List of observed galaxies in the XLSSJ0223 field and spectroscopic redshift measurements.

ID	RA (h:m:s)	Dec. (d:p:s)	F850LP (mag)	$i_{775} - z_{850}$ (mag)	Flag[a]	z_{spec}^{b}	Em[c]
4	02:23:09.381	−04:35:17.91	21.63 ± 0.01	0.89 ± 0.02	0	0.8992	–
377	02:23:09.428	−04:37:07.82	22.78 ± 0.03	1.06 ± 0.04	0	1.2154	[O II]
474	02:23:07.909	−04:36:45.16	23.32 ± 0.03	0.86 ± 0.04	−1	(0.9005)	–
537	02:23:08.485	−04:37:18.07	22.57 ± 0.02	0.99 ± 0.03	1	1.3153	[O II]
651	02:23:05.759	−04:36:10.27	21.62 ± 0.01	1.09 ± 0.02	1	1.2192	[Ne V]
962	02:23:05.420	−04:36:36.26	22.23 ± 0.02	1.02 ± 0.03	1	(1.2231)	–
972	02:23:04.718	−04:36:13.47	22.61 ± 0.03	0.92 ± 0.03	1	1.2153	–
983	02:23:04.843	−04:36:19.87	22.85 ± 0.02	0.94 ± 0.03	1	1.2149	–
1076	02:23:02.851	−04:35:40.02	21.52 ± 0.02	1.06 ± 0.03	0	1.0255	[O II]
1117	02:23:07.938	−04:34:46.03	24.09 ± 0.05	0.70 ± 0.07	−1	0.5286	[O II]
1142	02:23:03.262	−04:36:14.60	21.30 ± 0.01	1.00 ± 0.02	1	1.2204	–
1147	02:23:03.352	−04:36:15.64	22.56 ± 0.02	0.82 ± 0.03	−1	0.7615	Em
1175	02:23:03.242	−04:36:18.50	21.90 ± 0.02	1.08 ± 0.02	1	1.2201	[O II]
1193	02:23:02.799	−04:36:05.92	23.01 ± 0.03	1.07 ± 0.05	0	1.3890	–
1302	02:23:00.882	−04:35:39.85	23.29 ± 0.03	1.00 ± 0.04	1	–	–
1317	02:23:02.042	−04:36:32.17	21.37 ± 0.01	0.96 ± 0.02	−1	0.7330	–
1320	02:22:59.820	−04:35:12.25	23.52 ± 0.05	0.82 ± 0.07	0	(1.3342)	–
1370	02:23:02.021	−04:36:43.26	23.10 ± 0.03	0.96 ± 0.04	1	1.2249	–
1442	02:22:57.980	−04:36:22.31	21.88 ± 0.01	0.91 ± 0.02	0	1.2250	[O II]
1448	02:22:58.869	−04:36:49.89	23.94 ± 0.05	1.01 ± 0.07	1	1.2080	[O II]
1630	02:23:00.929	−04:36:50.19	21.48 ± 0.01	1.04 ± 0.02	1	1.2109	[O II]
1711	02:22:59.990	−04:36:02.53	20.92 ± 0.01	1.02 ± 0.02	1	1.2097	–

[a]Target priority: 1 – the target belongs to the sample of spheroids cluster member candidates (Saracco et al. 2017); 0 – the target is a spheroidal galaxy with photometric redshift compatible with the redshift of the cluster; −1 – the target is a filler galaxy best matching the remaining slit positions on the mask.

[b]Bracketed values are uncertain redshift, based only on the fit of the overall shape of the continuum; dots indicate undetermined redshift.

[c]Emission lines detected: dots – no emission line; Em – more than one emission line.

remaining five spheroidal galaxies cluster members. In the figures, the black curve is the 8-h MODS spectrum binned to 3.4 Å pixel^{-1}, the green curve is the best-fitting template. For each galaxy, the 2 × 2 arcsec ACS-F850LP image is also shown.

3 VELOCITY DISPERSION AND DYNAMICAL MASS

The galaxy stellar velocity dispersion σ_* is given by the relation $\sigma_*^2 = \sigma_{obs}^2 - \sigma_{inst}^2$, where σ_{obs} is the velocity dispersion measured on the observed spectrum and $\sigma_{inst} = 111$ km s^{-1} is the instrumental broadening resulting from the instrumental resolution ($R \simeq 1150$). The uncertainties on σ_* were derived by repeating the measurement for a set of 100 spectra obtained by summing to the best-fitting template, the real 1D residual background extracted from the final two-dimensional (2D) spectra, randomly shuffled in the wavelength range considered for measurement. We adopted, as uncertainty, the median absolute deviation (MAD) resulting from the distribution of the measurements.

The independence of the velocity dispersion measurements of the template library used was tested by repeating the fitting to the observed spectra with the set of synthetic stars used by Gargiulo et al. (2016), selected from the high-resolution ($R \sim 20\,000$) spectral library of Munari et al. (2005) and with a set of SSPs of Bruzual & Charlot (2003). These additional sets of templates returned values always within 8 per cent from the reference values with no systematic. The robustness of the measurements against the wavelength range considered was tested by repeating the fitting

considering different wavelength ranges of the spectrum. In all the cases considered, we obtained measurements well within the 1σ error. In Table 2, we report the values of the velocity dispersion σ_* and their errors. Since the measurements refer to 1.2 arcsec slit width and spectra were extracted within 0.9–1.1 arcsec, we scaled measurements to a radius $r = 0.6$ arcsec. In Table 2, we report also the velocity dispersion σ_e within the effective radius R_e obtained following the relation

$$\sigma_*/\sigma_e = (r/R_e)^{-0.065} \tag{1}$$

(Cappellari et al. 2006, see also Jørgensen, Franx & Kjaergaard 1995b).

The dynamical masses $\mathcal{M}_{dyn}$ of the galaxies have been derived from the velocity dispersions σ_e and the effective radii R_e according to the relation

$$\mathcal{M}_{dyn} = k_n \frac{\sigma_e^2 R_e}{G} \tag{2}$$

with $k_n = 5$, G is the gravitational constant, and k_n is the virial coefficient that takes into account the distribution of both luminous and dark matter (DM) and the projection effects (see e.g. Bertin, Ciotti & Del Principe 2002; Lanzoni & Ciotti 2003).

Cappellari et al. (2006), using a sample of local spheroidal galaxies, show that a value $k_n \simeq 5$ provides, on average, the best approximation to the real value at $z \sim 0$. Therefore, also for homogeneity with other data in the literature, we adopted this value of k_n in equation (2).

4 FP DETERMINATION

In the three-dimensional (3D) logarithmic space defined by the effective radius R_e (kpc), the central stellar velocity dispersion σ_0 (km s^{-1}), and the surface brightness $\langle I \rangle_e$ (L$_\odot$ pc^{-2}), usually evaluated within the half-light radius, elliptical galaxies are observed to be arranged along a plane known as FP (e.g. Djorgovski & Davis 1987; Dressler et al. 1987; Jørgensen, Franx & Kjaergaard 1996; Pahre, Djorgovski & de Carvalho 1998). The FP is usually expressed

in the form:

$$\log R_e = \alpha \log \sigma_0 + \beta \log \langle I \rangle_e + \gamma, \tag{3}$$

where α and β are the slopes and γ is the offset. The central velocity dispersion σ_0 is often corrected to an aperture of $R_e/8$. The coefficients of the FP only weakly depend on wavelength (e.g. Bernardi et al. 2003; La Barbera et al. 2010b), while they can significantly differ according to the fitting procedure adopted, as
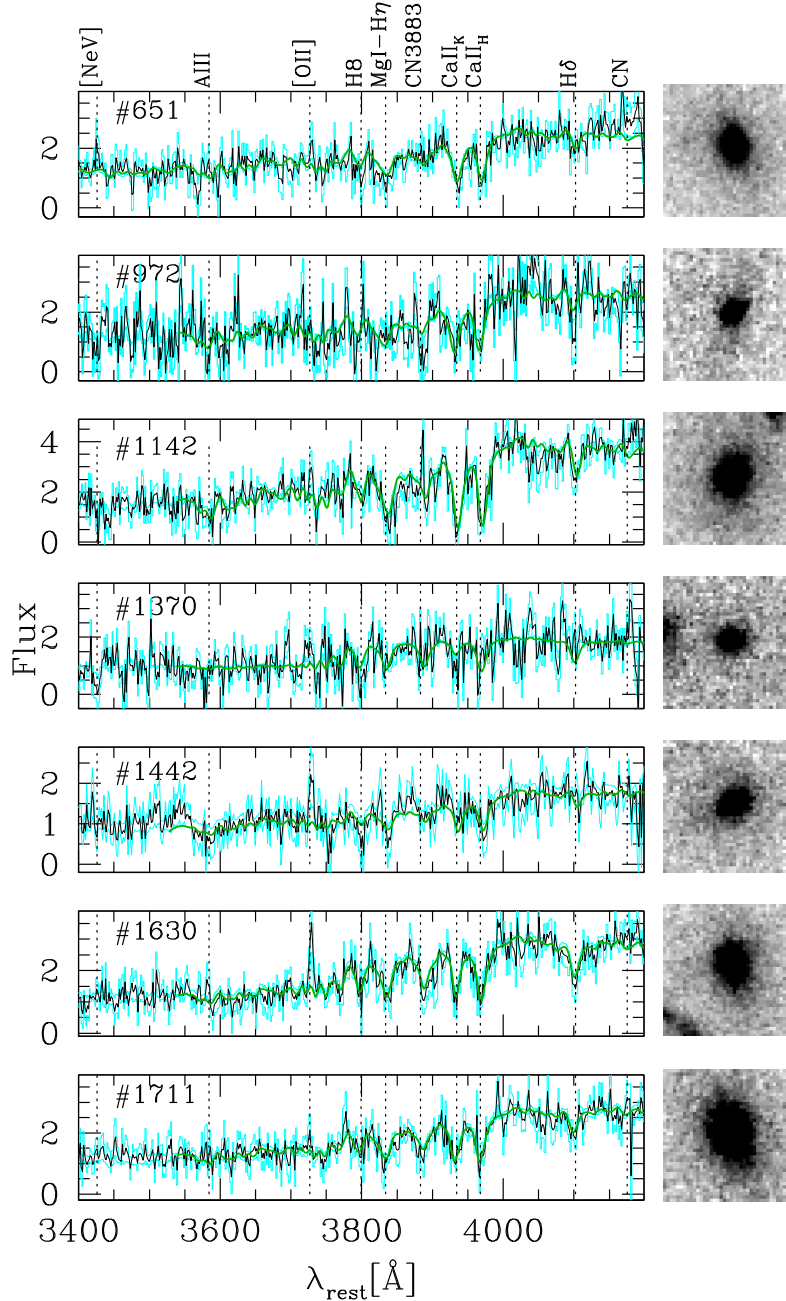
Figure 1. LBT-MODS spectra of the seven spheroidal galaxies cluster members for which velocity dispersion were measured. These spectra have S/N = [6–18] per Å in the galaxy rest frame, in the range 3900 < λ_{rest} < 4100 Å. The black curve is the observed spectrum binned to 3.4 Å pixel^{-1} as normalized by PPXF (flux is in arbitrary units). The green curve is the best-fitting MILES model resulting from the PPXF spectral fitting. Cyan histogram is the error ($\pm\sigma$) scaled by the same normalization factor of the spectrum to preserve the original S/N. The dotted vertical lines mark the main spectral features labelled on top of the figure. To the right of each spectrum, the ACS-F850LP image (2 × 2 arcsec) of the galaxy is shown.
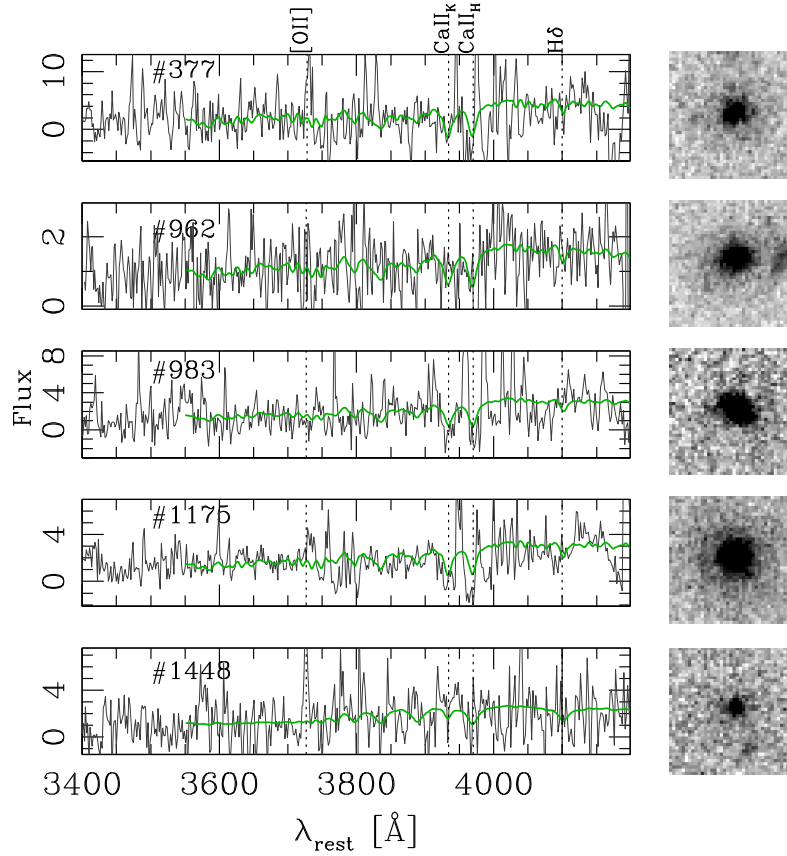
Figure 1. (Cont.). MODS spectra for the remaining six spheroidal cluster member galaxies for which only spectroscopic redshift was obtained.

Table 2. Structural and kinematic parameters of galaxies. Column 1: ID; column 2: stellar velocity dispersion; column 3: Sérsic index; column 4: circularized effective radius for Sérsic profile; columns 5 and 6: surface brightness and velocity dispersion within the Sérsic effective radius; columns 7–9: same as columns 4–6 but for de Vaucouleurs profile; column 10: dynamical mass (equation 2); column 11: stellar mass (from Saracco et al. 2017). It is worth noting that $\sigma_{e/8} = 1.132 \times \sigma_e$, according to equation (1). The extraction radius slightly varies from galaxy to galaxy in the range of 0.9–1.1 arcsec.

ID	σ_* (km s^{-1})	n_{Ser}	R_e^{F850} (kpc)	$\log\langle I_e\rangle$ (L$_\odot$ pc^{-2})	σ_e (km s^{-1})	$R_{e, Dev}$ (kpc)	$\log\langle I_{e, Dev}\rangle$ (L$_\odot$ pc^{-2})	$\sigma_{e, Dev}$ (km s^{-1})	$\log\mathcal{M}_{dyn}$ (M$_\odot$)	$\log\mathcal{M}_*$ (M$_\odot$)
651	215 ± 28	2.9 ± 0.3	3.5 ± 0.2	3.04 ± 0.02	220	5.1 ± 0.2	2.75 ± 0.02	215	11.29 ± 0.1	10.94
972	207 ± 47	6.5 ± 0.6	2.4 ± 1.5	3.02 ± 0.20	216	1.4 ± 0.1	3.79 ± 0.10	224	11.11 ± 0.1	10.54
1142	221 ± 38	5.4 ± 0.3	9.1 ± 1.1	2.40 ± 0.06	213	5.1 ± 0.2	3.33 ± 0.06	221	11.68 ± 0.1	11.50
1370	102 ± 90	3.8 ± 0.5	0.8 ± 0.2	3.72 ± 0.10	115	1.1 ± 0.2	3.80 ± 0.10	112	10.10 ± 0.5	10.08
1442	178 ± 69	6.5 ± 0.7	2.5 ± 0.4	3.26 ± 0.10	210	1.4 ± 0.1	3.76 ± 0.06	222	11.11 ± 0.4	10.90
1630	193 ± 50	5.3 ± 0.3	3.3 ± 0.3	3.12 ± 0.04	198	2.3 ± 0.1	3.74 ± 0.04	202	11.18 ± 0.1	10.75
1711	247 ± 23	6.0 ± 0.2	4.7 ± 0.3	3.08 ± 0.04	247	2.4 ± 0.1	3.94 ± 0.04	258	11.52 ± 0.2	11.20

discussed by, e.g., Saglia et al. (2001), Bernardi et al. (2003), La Barbera et al. (2010b), Sheth & Bernardi (2012), and Cappellari et al. (2013).

In this section, we compare the FP of cluster spheroidal galaxies at $z \sim 1.3$ with the one at $z \sim 0$ to constrain the evolution subtended in the last 9 Gyr. To perform a reliable comparison, we use the same fitting procedure for the high redshift and the local reference samples.

4.1 High-redshift sample

We combined the data of the cluster XLSSJ0223, with those collected by Jørgensen et al. (2014) for the cluster RXJ0848 (LinxW) at $z = 1.27$ and the velocity dispersion measurements obtained by Beifiori et al. (2017) for a sample of galaxies in the cluster XMMJ2235 at $z = 1.39$. For the cluster RXJ0848, following Jørgensen et al. (2014), we considered the eight spheroidal galaxies belonging to sample #5 in their table 7. The parameters of these galaxies are summarized in Table A1. For the cluster XMMJ2235, out of the nine galaxies observed by Beifiori et al. (2017), we considered the seven galaxies having spheroidal morphology, six of which previously studied in detail by Ciocca et al. (2017). The parameters of these galaxies are summarized in Table A2.

The high-redshift sample is thus composed of 22 cluster spheroidal galaxies in the redshift range $1.2 < z < 1.4$. The parameters of all the galaxies in these three clusters have been homogeneously derived using Galfit on ACS-F850LP images, sampling the rest-frame B band at the redshift of the clusters. In particular, photometry and structural parameters of galaxies have been derived and studied by Saracco et al. (2014) for cluster

RXJ0848, by Ciocca et al. (2017) for cluster XMMJ2235, and by
Saracco et al. (2017) for cluster XLSS0223. Jørgensen et al. (2014)
find a good agreement between their measurements for cluster
RXJ0848 and those by Saracco et al. (2014). Analogously, Ciocca
et al. (2017) find a good agreement between their measurements for
cluster XMMJ2235 and those by Chan et al. (2016) for the same
cluster (see also the Appendix for further information).

4.2 Local reference samples

As reference local samples, we considered the Coma cluster sample
of Jørgensen et al. (1995b) and the Shapley sample of Gargiulo
et al. (2009). The Coma cluster sample is composed of the 74
spheroidal galaxies with stellar velocity dispersion measurements
(Jørgensen et al. 1995b) and structural parameters derived from
$r^{1/4}$ profile fitting in the r-Gunn filter (Jørgensen et al. 1995a). We
derived the corrections to apply to the parameters in the r band to
obtain those in the B band, using the sample of 28 ellipticals in
the cluster for which measurements were performed also in the B
band (Jørgensen et al. 1995a). The effective radius in the B band
is obtained by scaling the effective radius in the r band by the
mean ratio $\langle r_{e,B}/r_{e,r}\rangle = 1.05 \pm 0.08$. The B-band surface brightness
in physical units, $\log\langle I_e\rangle = -0.4\mu_e + 10.8$ [$L_\odot$ pc^{-2}], has been
derived from the surface brightness $\mu_e = r + \langle B-r\rangle + 5\log(r_{e,B}) +
2.5\log(2\pi)$, where $\langle B-r\rangle = 1.14 \pm 0.07$ is the mean colour of the
28 ellipticals. The Shapley sample is composed of 141 spheroidal
galaxies, whose structural parameters were derived through Sérsic
profile fitting in the R band (Gargiulo et al. 2009). The effective radii
in the B band were obtained by applying the same scaling factor
derived for the Coma galaxies (given the small different wavelength
between r and R), while the B-band surface brightness was derived
by applying to the R-band magnitude, the mean colour correction $B
- R = 1.57$ of local elliptical galaxies (e.g. Fukugita, Shimasaku &
Ichikawa 1995).

4.3 The FP at $z \sim 1.3$

Before proceeding, we assessed possible selection effects in the
high-redshift spectroscopic sample that may affect the analysis.
To this end, we compared the spectroscopic sample of 22 spheroids
cluster members with the photometric sample of 55 spheroids mem-
ber candidates of the three clusters at $z \sim 1.3$ (Saracco et al. 2017)
to which the 16 spectroscopic members belong. Fig. 2 shows the
distribution of the galaxies on the $\log\langle I_e\rangle$ versus $\log(R_e)$ plane, that is
the Kormendy relation. The high-redshift spectroscopic sample (red
filled points) follows the same [$\log\langle I_e\rangle$; $\log(R_e)$] distribution of the
photometric sample (red open squares). This is confirmed by the 2D
Kolmogorov–Smirnov (KS) test that gives a probability $P = 0.42$
that the two samples are extracted from the same parent population.
Thus, no obvious bias affecting size and/or surface brightness is
present in the high-redshift spectroscopic sample.

   We derived the best-fitting relation $\log(I_e) = a \times \log(R_e) + b$
by using orthogonal fit. We obtained $a = -1.5 \pm 0.3$ and $b =
3.9 \pm 0.2$ for the high-redshift sample and $a = -1.3 \pm 0.1$ and
$b = 3.04 \pm 0.06$ for the low- redshift sample. Given the correlated
errors between $\langle I_e\rangle$ and R_e, we repeated the fitting also using the
routine linmix_err (Kelly 2007) that applies a Bayesian method
to account for correlated measurement errors in linear regression.
The resulting best-fitting relations are summarized in Table B1.
No significant differences are found with respect to the relations
obtained with the orthogonal fit. We notice that the orthogonal fit
has been proved to be robust with respect to outliers (e.g. Jørgensen
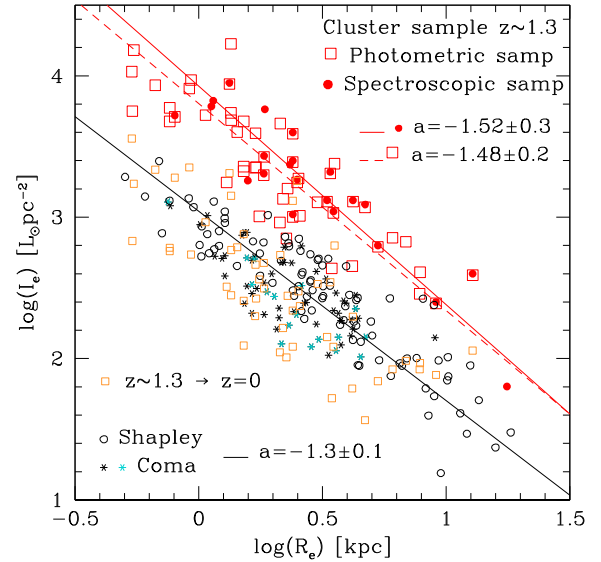
Figure 2. Kormendy relation of spheroidal galaxies in cluster. Skeletal
symbols are the Coma cluster galaxies (cyan symbols are galaxies younger
than 7 Gyr, see the text) (Jørgensen et al. 1995b; Jørgensen, Franx &
Kjaergaard 1995a); open circles are the galaxies in the Shapley sample
(Gargiulo et al. 2009); filled red symbols are the 22 spheroids of the cluster
sample at $z \sim 1.3$ (Section 4.1); large red open squares are the photometric
sample of 55 spheroids cluster member candidates at $z \sim 1.3$ (Saracco et al.
2017), to which the 16 spectroscopic members belong to; small open orange
squares are the spheroids passively evolved to $z = 0$. The best-fitting relation
$\log(I_e) = a \times \log(R_e) + b$ obtained through orthogonal fit is shown.

et al. 1996) treating all the variables symmetrically, and has been
adopted in many previous studies (see e.g. La Barbera et al. 2010a).
For this reason, while comparing our results to those obtained with
the Kelly's method, we adopt the orthogonal fit as our reference
fitting throughout this work.

   We tried to account for the progenitor bias (e.g. van Dokkum
et al. 2001; Carollo et al. 2013), identifying galaxies in the Coma
sample potentially too young to be descendants of high-redshift
galaxies. To this end, we used the estimates based on line-strength
indices by Harrison et al. (2010) that provide ages for 43 galaxies
($\sim$60 per cent) of the Coma sample here considered. Seventeen
galaxies out of the 43 ($\sim$40 per cent) are younger than 7 Gyr. Thus,
other $\sim$10 galaxies younger than this age could be expected among
the remaining galaxies.[1] We choose 7 Gyr as limiting age instead of
the lookback time $t_{LB}(z = 1.3) \sim 8.5$ Gyr, to leave room to spheroids
that may have experienced a secondary burst of star formation
at later times. These young galaxies are highlighted in cyan in
Fig. 2. The best-fitting relation obtained without considering young
galaxies ($a = -1.4 \pm 0.3$, $b = 2.9 \pm 0.2$) does not significantly
differ from the one obtained considering the whole sample. We
further discuss the Kormendy relation below.

   Fig. 3 shows two different views of the data in the 3D space $\log\sigma$,
$\log\langle I_e\rangle$, $\log(R_e)$. To homogenize, the low-z samples, we considered
for the Shapley sample only galaxies (92) with $\sigma > 100$ km s^{-1}. The
two different views show that the high-z data (red points) are offset

---

[1]It is worth noting that the light-weighted age derived from H β index, as
in the case of Harrison et al. (2010), is strongly affected by recent episodes
of star formation. Hence, on average, it is biased towards ages younger than
the true age of the bulk of stars. Therefore, 40 per cent should be considered
an upper limit to the fraction of young galaxies.
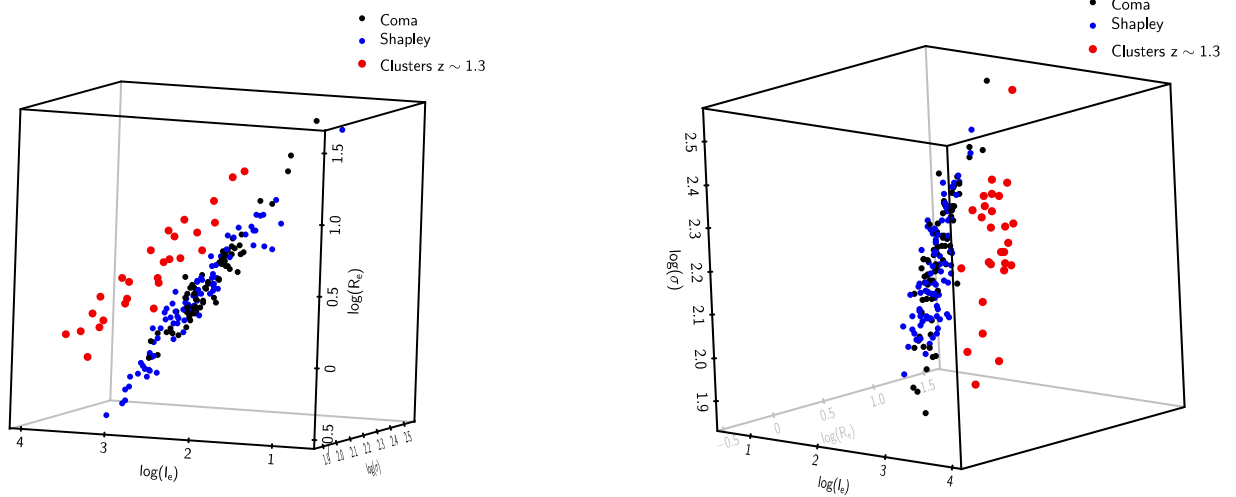
Figure 3. 3D views in the $\log(\sigma)$, $\log\langle I_e\rangle$, $\log(R_e)$ space of the low- and high-z cluster data. Black dots are the Coma data, blue dots are the Shapley data, and red dots are the data of the three clusters at $z \sim 1.3$.

with respect to the local data (blue and black points) and define a plane with different slope. In Fig. 4, we plot the so-called long and short edge-on projections of the FP (see e.g. Jørgensen et al. 1995b). We considered the velocity dispersion $\sigma_{e/8}$ scaled to $R_e/8$ and parameters derived from Sérsic profile fitting for all the samples, with the exception of the Coma cluster sample whose parameters are derived from Devaucoulers profile. The figures show the two edge-on views of the FP for the spheroidal galaxies in the three clusters at $z \sim 1.3$ and for the local reference samples, assuming the values $\alpha = 1.3$ and $\beta = 0.82$ in equation (3) (Jørgensen et al. 2006). Also in this case, it is visible the different slopes of the plane defined by the high-redshift cluster sample with respect to local ones.

A rotation of the FP at high z is still a controversial issue. While some authors find evidence of an evolution of the parameters α and β since $z = 0.8$–0.9 (e.g. Treu et al. 2005a, b; di Serego Alighieri et al. 2005; Jørgensen et al. 2006; Jørgensen & Chiboucas 2013; Woodrum et al. 2017), other authors do not detect significant variation at similar redshift (e.g. Holden et al. 2010). Different slopes imply a differential evolution of the population of elliptical galaxies along the plane: the mean properties of the population change over time along the plane in a different way according to the position on the plane, i.e. according to the physical parameters mass and/or size, and/or to the stellar population properties.

We constrained the evolution of the FP applying the same fitting procedure to the low-redshift and the high-redshift data. The best-fitting coefficients α, β, and γ of equation (3) have been determined using the code `lts_planefit` (Cappellari et al. 2013) that performs a robust linear regression with errors in all variables. We first established the FP in the local Universe as reference. For the Coma cluster galaxies, whose parameters were derived from de Vaucoulers profile, we obtained $\alpha = 1.27(\pm 0.07)$, $\beta = -0.87(\pm 0.03)$, and $\gamma = 0.46(\pm 0.01)$ with an rms of 0.07, not significantly different from the relation found by Jørgensen et al. (2006) in the B band. By excluding galaxies younger than 7 Gyr, we obtained $\alpha = 1.34(\pm 0.07)$, $\beta = -0.89(\pm 0.03)$, and $\gamma = 0.48(\pm 0.01)$. For the Shapley galaxies, whose parameters were derived from Sérsic profile, we obtained $\alpha = 1.12(\pm 0.09)$, $\beta = -0.78(\pm 0.02)$, and $\gamma = 0.46(\pm 0.01)$ with an rms of 0.09, not significantly different from the relation found by Gargiulo et al. (2009). The best-fitting relations obtained for the local samples are shown in Fig. C1. By fitting the 22 cluster spheroids at $z \sim 1.3$ with

structural parameters derived from Sérsic profile fitting, we obtain

$$\log R_e = 1.3(\pm 0.4)\log\sigma_{e/8} - 0.49(\pm 0.08)\log\langle I\rangle_e + 0.4(\pm 0.1) \quad (4)$$

with an rms of 0.05. The best fit is shown in Fig. C2. Considering $r^{1/4}$ profile fitting, we obtain $\alpha = 1.0(\pm 0.2)$ and $\beta = -0.34(\pm 0.03)$. We verified that excluding from the fitting galaxy #1370, whose velocity dispersion has a large uncertainty (see Table 2), does not affect significantly the FP best-fitting coefficients in equation (4).

The variation of α is not statistically significant, given the large uncertainty affecting this parameter. On the contrary, the variation of β, $\Delta\beta > 0.29(\pm 0.08)$, seems to be significant, a conclusion reached also when $r^{1/4}$ profile is considered. We checked whether correlated errors between R_e and $\langle I_e\rangle$ can affect this result by repeating the fitting of the FP to 100 simulated samples of 22 galaxies, even if we already verified that correlated errors does not affect the relation between these two parameters (Fig. 2 and Table B1). We considered $r^{1/4}$ measurements to directly compare the result with the Coma FP parameter ($\beta = -0.87 \pm 0.03$). The values of R_e and L_B of each galaxy have been varied by adding a shift randomly chosen from Gaussian distributions with sigmas dR_e and dL_B, respectively, where dR_e and dL_B are the errors on the two parameters. Then, a new value of I_e has been derived from these perturbed values and assigned to the galaxy (see also the Appendix).

In Fig. 5, the distribution of the best fitting α and β values obtained for the 100 simulated samples are shown. We confirm that the effect of the correlated errors is very weak ($\sim$10 per cent) in agreement with what already shown in La Barbera et al. (2010b). The simulations provide a median value $\langle\alpha\rangle = 0.93 \pm 0.14$ and $\langle\beta\rangle = -0.35 \pm 0.04$, confirming a variation of this latter parameter at the $\sim 3\sigma$ level. Thus, in agreement with, e.g., Treu et al. (2005a), Treu et al. (2005b), di Serego Alighieri et al. (2005), Jørgensen et al. (2006), Jørgensen & Chiboucas (2013), and Woodrum et al. (2017), but at variance with others, e.g. Holden et al. (2010), our analysis shows a rotation of the FP at $z \sim 1.3$ with respect to the local plane.

5 THE M/L RATIO

In Fig. 6, galaxies are plotted on the M_{dyn}/L_B versus M_{dyn} plane (left) and M_{dyn}/L_B versus σ_e (right) plane, another way to represent the FP projections, where the mass M_{dyn} is given by equation (2). As
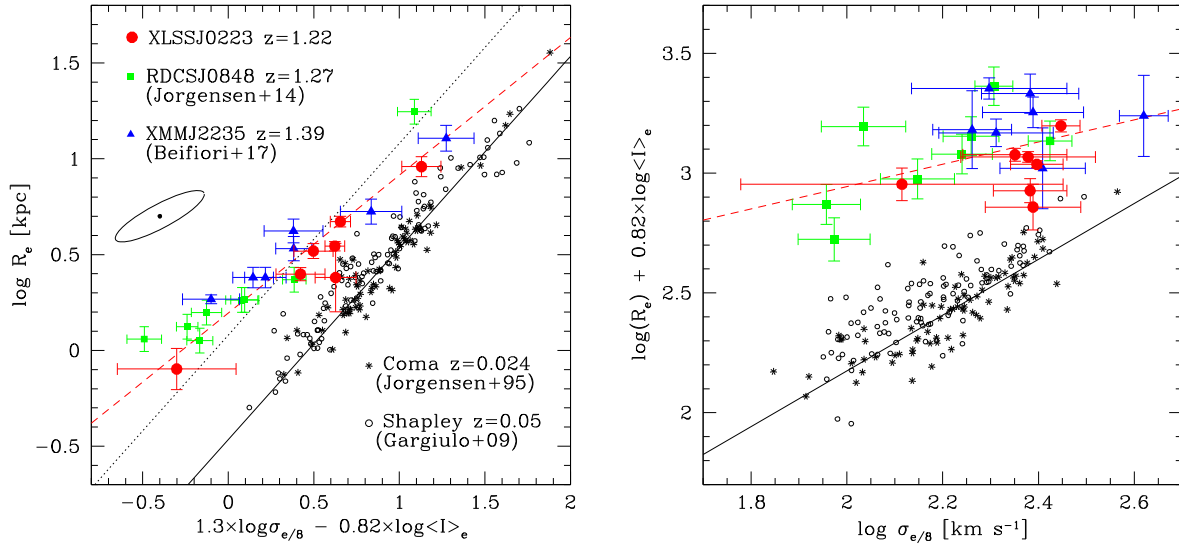
Figure 4. Edge-on views of the *B*-band FP of spheroidal galaxies in cluster. Skeletal symbols are the 74 galaxies of the Coma cluster sample (Jørgensen et al. 1995a, b, see details in the text); open circles are the 92 galaxies in the Shapley sample with $\sigma > 100$ km s^{-1} (Gargiulo et al. 2009); filled symbols are the 7 galaxies in the cluster XLSS0223 (red circles, this work), the 8 galaxies in the cluster RDCS0848 (green symbols; Jørgensen et al. 2014), and the 7 galaxies in the cluster XMMJ2235 (blue triangles; Beifiori et al. 2017). The black solid lines are the best-fitting relation to the Coma cluster sample. The black dotted line in the left-hand panel is the best fit to the Coma data offset to the mean zero-point of the high-*z* data. The red dashed lines are the best fit to the high-*z* data when the values $1.3\log(\sigma)$ and $0.82\log\langle I_e\rangle$ are considered. Note that the error bars on the left plot should not be crosses but rather tilted ellipses due to the correlated errors between R_e and I_e, as shown by the ellipse representing the typical (mean) contour level at 1σ.

expected, the best-fitting relation (orthogonal fit)[2] of high-redshift spheroids
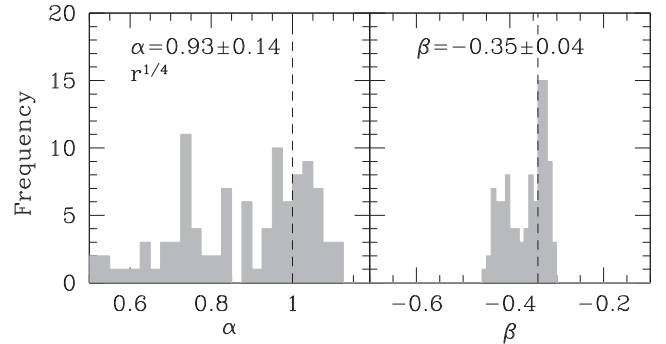
$$\log(M_{dyn}/L_B) = (0.6 \pm 0.1)\log(M_{dyn}) - (6.2 \pm 0.5) \quad (5)$$

is steeper than the local one

$$\log(M_{dyn}/L_B) = (0.26 \pm 0.03)\log(M_{dyn}) - (2.13 \pm 0.06) \quad (6)$$

as also previously found by other authors (e.g. Treu et al. 2005a, b; di Serego Alighieri et al. 2005; Jørgensen et al. 2006; Saglia et al. 2010; Jørgensen & Chiboucas 2013; van de Sande et al. 2015; Woodrum et al. 2017). In Table B1, we report the relations obtained considering the correlated errors among M_{dyn}/L_B, M_{dyn} and σ_e in the fitting. Also in this case, no significant differences are found with respect to the relations obtained through orthogonal fitting. The different slope obtained for high- and low-redshift samples implies that M_{dyn}/L_B has changed over time in a different way for lower mass and higher mass galaxies.

Trends visible in Fig. 6 can be due to a differential evolution of individual galaxies to different properties of the spheroids joining the population at later times, or to a mix of these two causes. The relationships between stellar population properties (such as metallicity and age) and mass (e.g. Trager et al. 2000; Thomas et al. 2005; Gallazzi et al. 2014; McDermid et al. 2015; Jørgensen et al. 2017; Saracco et al. 2019) imply a mass-dependent evolution of the M_{dyn}/L_B ratio, even in the case that structural parameters of individual galaxies (σ and R_e, and hence M_{dyn}) do not change over time. These correlations imply a mass-dependent evolution of L_B and, consequently, of M_{dyn}/L_B. Moreover, metallicity and age seem to be also correlated to the stellar mass density of galaxies (e.g. Saracco, Longhetti & Gargiulo 2011; Tacchella et al. 2017; Saracco et al. 2019) that seems to be connected to the duration of

---

[2]It is worth to note that the error on the *b* parameter has been obtained by fitting the relation $y = a \log(x/\langle x\rangle) + b$ (e.g. Tremaine et al. 2002).

Figure 5. Distribution of the best-fitting α and β values obtained for the 100 simulated samples in case of $r^{1/4}$ profile. The dashed line represents the best-fitting values $\alpha = 1.0 \pm 0.2$ and $\beta = -0.34 \pm 0.03$ obtained for the true high-*z* cluster sample ($r^{1/4}$ profile). The median value and the MAD of the distributions are $\langle\alpha\rangle = 0.93 \pm 0.14$ and $\langle\beta\rangle = -0.35 \pm 0.04$.
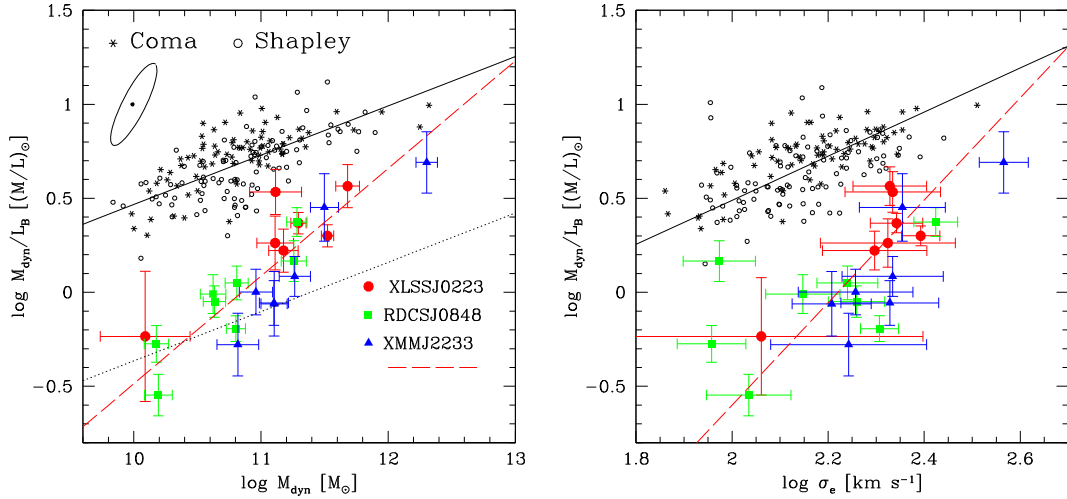
the star formation (Gargiulo et al. 2009). Therefore, we also expect a differential evolution of M_{dyn}/L_B versus mass density as a function of redshift.

5.1 The evolution of M_{dyn}/L_B

We first consider the case of no evolution of the FP slope to compare our results with those in the literature, then we consider the change of the slope.

The offset from the local relationship shown in Fig. 6 is usually used to measure the mean M_{dyn}/L_B evolution, under the assumption that α and β do not change with redshift. In this case, from equation (3), the offset of each galaxy is $\Delta\gamma_i = \gamma_{i,z} - \gamma_0 = \beta(\log(I_{e,0}/I_{ei,z}))$ that can be rewritten as $\Delta\log(M_{dyn,i}/L_{B,i}) = \Delta\gamma_i/\beta$. The mean (median) value of the individual $\Delta\log(M_{dyn,i}/L_{B,i})$ values

Figure 6. Dynamical mass-to-light ratio M_{dyn}/L_B versus dynamical mass M_{dyn} (left) and velocity dispersion σ_e (right) for high-redshift and low-redshift cluster spheroids. Lines are the best-fitting relations $\log(M/L) = a \log(M) + b$ and $\log(M/L) = a_\sigma \log(\sigma) + b_\sigma$ obtained with orthogonal fit to the low-redshift data (black solid line, $a = 0.26 \pm 0.03$ and $b = -2.13 \pm 0.06$; $a_\sigma = 1.2 \pm 0.1$, and $b_\sigma = -1.82 \pm 0.05$) and to the high-redshift data (red dashed line, $a = 0.6 \pm 0.1$ and $b = -6.2 \pm 0.5$; $a_\sigma = 2.7 \pm 0.5$ and $b_\sigma = -6.1 \pm 0.4$). The best-fitting relations obtained considering the correlated errors between the variables are reported in Table B1. Dotted line in the left-hand panel is the local relation offset to the median $\log(M_{dyn}/L_B)$ value of high-redshift data. Error bars should not be crosses but rather tilted ellipses, due to the correlated errors between M_{dyn}/L_B, M_{dyn} and σ_e, as shown by the ellipse plotted in the left-hand panel representing the typical (mean) 1σ confidence contour.

will result in the mean (median) M_{dyn}/L_B variation of the population of galaxies. It is worth to note that this $\Delta\log(M_{dyn}/L_B)$ derived from the FP is not necessarily the same shown in Fig. 6, where M_{dyn} comes from the virial theorem (equation 2).

We assumed, as reference, the coefficients of the local FP derived in Section 4.3 [$\alpha = 1.27$, $\beta = -0.87$] for Coma and [$\alpha = 1.12$, $\beta = -0.78$] for the Shapley sample. We derived the offset $\Delta\gamma_i$ by computing for each individual galaxy at $z \sim 1.3$ the quantity $\gamma_{i,z} = \log(R_{e,i}) - \alpha \log(\sigma_{e,i/8}) - \beta \log(I_{e,i})$ (e.g. Jørgensen et al. 2006; Saglia et al. 2010; La Barbera et al. 2010b). Fig. 7 shows $\Delta\log(M_{dyn}/L_B)$ for the high-redshift spheroids. The resulting median variation with respect to Coma is $\Delta\log(M_{dyn}/L_B) = -0.7 \pm 0.1$ that does not differ significantly from $\Delta\log(M_{dyn}/L_B) = -0.6 \pm 0.1$ obtained considering Shapley as reference. These values agree with the luminosity evolution $\Delta\log(I_e) = -0.72 \pm 0.1$, resulting from the Kormendy relation shown in Fig. 2 and also found by Jørgensen et al. (2014; $\Delta\log(I_e) = -0.77$).

The resulting evolution with redshift of M_{dyn}/L_B of cluster spheroids is $\Delta\log(M_{dyn}/L_B) = (-0.5 \pm 0.1)z$, (filled black triangle), in agreement with many previous estimates (e.g. van Dokkum & Stanford 2003; van Dokkum & van der Marel 2007; van der Marel & van Dokkum 2007; Holden et al. 2010; Saglia et al. 2010; Jørgensen et al. 2014; Beifiori et al. 2017; Prichard et al. 2017). We do not detect significant differences in the evolution of M_{dyn}/L_B of individual clusters. We obtained $\Delta\log(M_{dyn}/L_B) = (-0.45 \pm 0.1)z$, $\Delta\log(M_{dyn}/L_B) = (-0.54 \pm 0.1)z$, and $\Delta\log(M_{dyn}/L_B) = (-0.51 \pm 0.1)z$ for XLSSJ0223, RDCS0848, and XMMJ2235, respectively. This result supports our approach of analysing simultaneously all galaxies in the three clusters, when deriving the FP relation at $z \sim 1.3$ (Section 4.3).

Fig. 7 shows quantitatively the dependence of the M/L variation with redshift on dynamical mass. We divided the sample between low-mass galaxies having $\log(M_{dyn}) < 11.1$ $M_\odot$ and high-mass galaxies with $\log(M_{dyn}) \geq 11.1$ $M_\odot$, being $\log(M_{dyn}) = 11.1$ $M_\odot$ the median value of the whole sample. High-mass galaxies [median mass $\log(M_{dyn}) = 11.27$ $M_\odot$] are characterized by a milder evolution $\Delta\log(M_{dyn}/L_B) = (-0.38 \pm 0.07)z$ than low-mass
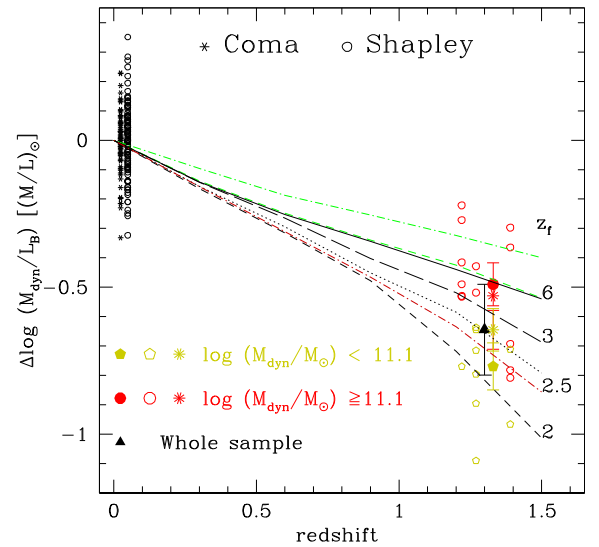
Figure 7. Offset of $\log(M_{dyn}/L_B)$ from the local value for the high-redshift spheroids coded by dynamical mass as in the legend of the figure. Filled black triangle is the median value $\Delta\log(M_{dyn}/L_B) = -0.6 \pm 0.1$ of the high-redshift sample. Coloured filled symbols (offset by 0.03 in z for clarity) are the median $\Delta\log(M_{dyn}/L_B)$ values of the M_{dyn}-selected subsamples. The skeletal symbols are the median $\Delta\log(M^*/L_B)$ values for the M_{dyn} selected. The black curves are the expected $\Delta\log(M^*/L_B)$ from BC03 SSPs (Bruzual & Charlot 2003) with Chabrier IMF and solar metallicity for different formation redshift z_f. The dark-red curve was obtained for $z_f = 2.5$ as the dotted line, but for metallicity $Z = 2.5Z_\odot$. The green curves were obtained for $z_f = 6$, Salpeter IMF (dashed curve; i.e. a single power law with index $s = 2.35$) and for a single power-law IMF with slope $s = 3.5$ (dot–dashed curve).

galaxies [median mass $\log(M_{dyn}) = 10.63$ $M_\odot$], whose variation is $\Delta\log(M_{dyn}/L_B) = (-0.59 \pm 0.08)z$.

From equations (5) and (6), one obtains the differential evolution of the M_{dyn}/L_B between low- and high-redshift galaxies as a function
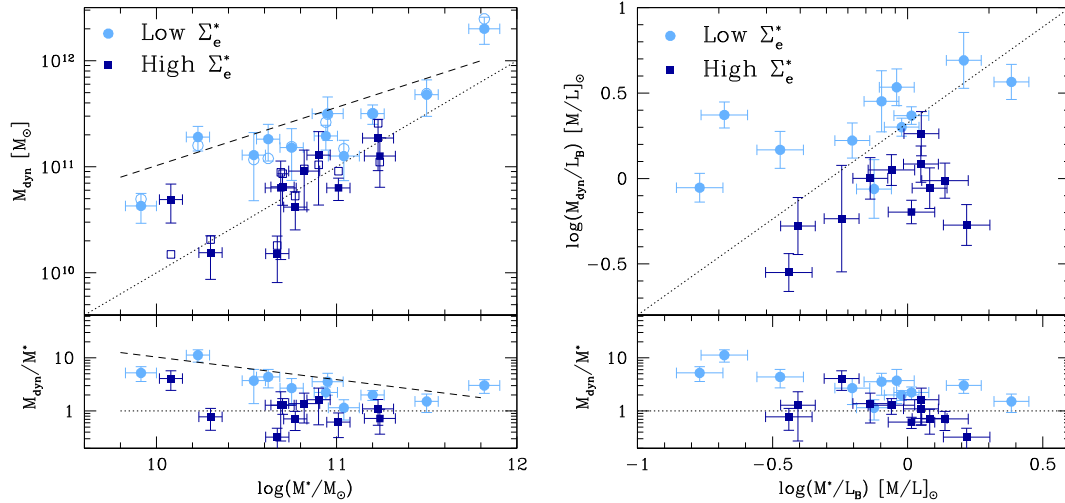
Figure 8. Left: Relation between dynamical mass M_{dyn}, as derived from equation (2), and stellar mass M^* for the 22 cluster spheroids at $z \sim 1.3$. Galaxies are coded according to their stellar mass density Σ_e^* (see Section 5): light-blue filled circles are low-density galaxies, with stellar mass density lower than the density median value of the sample; navy filled squares are high-density galaxies. The dotted line is the 1:1 relation, the dashed line is the upper relation enclosing 90 per cent of the data. The open symbols represent the dynamical mass obtained using the virial coefficient $\beta(n) = 8.87 - 0.831n + 0.0241n^2$ (Cappellari et al. 2006), where n is the Sérsic index. The lower panel shows the dynamical to stellar mass ratio as a function of stellar mass. It is worth to remind that error bars on M_{dyn}/M^* would be tilted ellipses because of the correlation with M^*. The median value of the ratio is $\langle M_{dyn}/M^* \rangle = 1.6 \pm 0.2$. Symbols are as in the upper panel. Right: Relation between the dynamical mass-to-light ratio M_{dyn}/L_B versus $M*/L_B$.

of galaxy mass:

$$\Delta \log(M_{dyn}/L_B) = (-0.34 \pm 0.1)\log(M_{dyn}) + (3.8 \pm 0.5). \quad (7)$$

The differential evolution derived considering the best-fitting relations obtained with `linmix_err` does not differ significantly (see Table B1). This trend is consistent with that found by Jørgensen et al. (2006) for cluster spheroids at $z \sim 0.9$, and reflects the fact that the M_{dyn}/L_B–mass relation is steeper for high-relative to low-redshift galaxies, consistent with the redshift evolution of the FP slopes.

5.2 The formation redshift of cluster spheroids

If the variation of the M_{dyn}/L_B was only due to the evolution of the stellar populations over time and $M_{dyn}/M^* = $ cost, then $\Delta \log(M_{dyn}/L_B) = \Delta \log(M^*/L_B)$. In this case, using SSP models, this variation can be translated into the epoch of the last major episode of star formation, i.e. the formation redshift z_f of the bulk of the stellar mass.

In Fig. 7, the predicted $\Delta \log(M^*/L_B)$ values for the SSP models of Bruzual & Charlot (2003, BC03) are shown for different values of z_f and Chabrier initial mass function (IMF) and compared to the observed $\Delta \log(M_{dyn}/L_B)$ of high-redshift galaxies. Black curves are obtained with solar metallicity, while the dark-red dashed curve (obtained for $z_f = 2.5$, as the black dotted curve) is obtained for $Z = 2.5Z_\odot$ to show the effect of the metallicity. For comparison, the green-dashed curve ($z_f = 6$, $Z_\odot$) was obtained with a Salpeter IMF (i.e. a single power-law IMF functional form, with slope $s = 2.35$), while the dot–dashed curve refers to the bottom-heavier IMF with $s = 3.5$ (i.e. a distribution with a strong contribution from low-mass stars).

Under the assumptions above, the resulting median formation redshift of the stellar populations for the whole population of high-redshift spheroids (black filled triangle) is $z_f \simeq 2.5$ for $Z = Z_\odot$ ($z_f \simeq 2.7$ for $Z = 2.5Z_\odot$). This agrees with the formation redshift obtained from stellar absorption line strengths and full spectral fitting for the 7 spheroids in the cluster XLSSJ0223 (Saracco et al.

2019) and with what found by Beifiori et al. (2017) for cluster XMMJ2235.

Fig. 7 shows also that stellar populations in high-mass [$\log(M_{dyn} > 11.1\ M_\odot$)] spheroids form earlier ($z_f \simeq 6$) than those in lower mass spheroids ($z_f \sim 2.2$), in agreement with many previous works (e.g. Thomas et al. 2010). A better estimate of z_f as a function of galaxy mass can be obtained from equation (7), which reflects the evolution with redshift of the FP slopes. Interpreting the variation of M_{dyn}/L_B of equation (7) as a difference in the epoch of the last major star formation episode, we obtain

$$\log(age(z_f)) = (-0.39 \pm 0.1) \times \log(M_{dyn}) + (4.4 \pm 0.6), \quad (8)$$

where we used the best-fitting relation $\log(M^*/L_B) = 0.86\log(age)$ obtained for BC03 models (Chabrier IMF, $Z_\odot$). This implies that a galaxy with mass $\log(M_{dyn}) \geq 11.5\ M_\odot$ has experienced its last burst when the Universe was ≤ 0.82 Gyr old, i.e. at $z_f \geq 6.5$, while a galaxy with $\log(M_{dyn}) \leq 10\ M_\odot$ at $z_f \leq 2$.

The same trend is qualitatively obtained considering M^*/L_B instead of M_{dyn}/L_B. This is shown by the skeletal symbols in Fig. 7 that represent the median $\Delta \log(M^*/L_B)$ values of low-M_{dyn} and high-M_{dyn} spheroids. The median $\Delta \log(M^*/L_B)$ values have been obtained by summing to $\Delta \log(M_{dyn}/L_B)$ the median $\log(M_{dyn}/M^*) = \log(M_{dyn}/L_B) - \log(M^*/L_B)$ values obtained for low-M_{dyn} and high-M_{dyn} galaxies. The M^*/L_B-based formation redshifts of the stellar populations in low- and high-mass spheroids differ, to some extent, with respect to those obtained considering $\Delta M_{dyn}/L_B$. This shows that the assumption $\Delta \log(M_{dyn}/L_B) = \Delta \log(M^*/L_B)$ does not match the real case and suggests a variation of M_{dyn}/M^* among the population of spheroids.

Fig. 8 (left) shows the relation between M_{dyn} and M^* for the high-redshift spheroids coded according to their stellar mass density $\Sigma_e^* = M^*/(2\pi R_e^2)$: low-density spheroids (light blue pentagons) have $\Sigma_e^* < \Sigma_{med}^* \simeq 1800\ M_\odot\ pc^{-2}$ (the median Σ_e^* of the sample); high-density spheroids (dark blue points) have $\Sigma_e^* > \Sigma_{med}^*$. The overall best-fitting relation is $\log(M_{dyn}) = (1.09 \pm 0.2)\log(M^*) - (0.7 \pm 1.3)$. The median value of the whole sample is
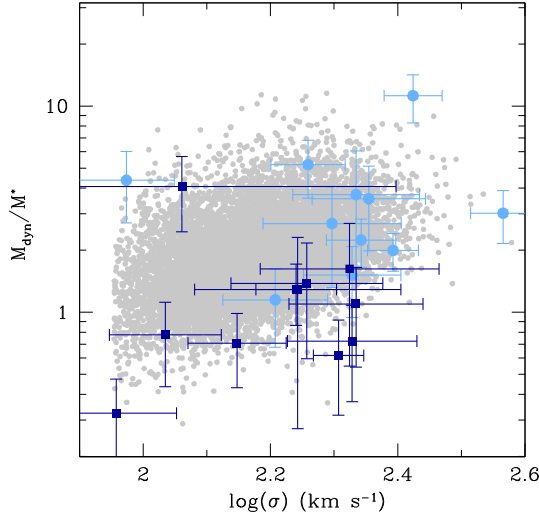
Figure 9. M_{dyn}/M^* is plotted versus the stellar velocity dispersion for the 22 spheroidal galaxies in cluster at $z \sim 1.3$ (blue and light-blue symbols) coded according the their stellar mass density and for a sample of local spheroids (grey symbols) extracted from the SPIDER sample (La Barbera et al. 2010a). Also in this case, errors would be tilted ellipses (see e.g. Fig. 4) because of the correlation between M_{dyn} and σ.

$\langle M_{dyn}/M^* \rangle = 1.6 \pm 0.2$. We note that one galaxy, #1264 belonging to the cluster RXJ0848 has $M_{dyn}/M^* < 1$. This galaxy has the lowest velocity dispersion ($\sim$90 km s^{-1}) with a small error and a relatively high stellar mass (see Table A1). We cannot exclude a systematicity in one of these measurements. Two trends are visible: at fixed stellar mass, lower density spheroids have systematically higher M_{dyn}, hence larger M_{dyn}/M^*; the mean M_{dyn}/M^* of low-Σ^* galaxies ($\langle M_{dyn}/M^* \rangle_{l\Sigma} = 3.0 \pm 1$) increases for decreasing stellar masses and tends to the nearly constant value $\langle M_{dyn}/M^* \rangle_{h\Sigma} = 1.1 \pm 0.3$ of high-Σ^* galaxies at large stellar masses. These trends do not depend on the virial mass estimator adopted (equation 2), as shown by the open symbols representing $M_{dyn} = \beta(n)\sigma_e^2 R_e/G$, where $\beta(n) = 8.87 - 0.831n + 0.0241n^2$ (Cappellari et al. 2006) and n is the Sérsic index.

Some evidences have been accumulated in favour of a variation of the IMF with velocity dispersion (e.g. La Barbera et al. 2013), or mass density (at constant dark matter (DM) fraction, e.g. Gargiulo et al. 2015) or mass of galaxies [see the Introduction section in De Masi et al. (2019) for a concise review]. Some of these studies consider the IMF normalization ratio M^*_{dyn}/M^*, often called Γ, as a comparison between stellar mass M^*, obtained for a reference IMF (e.g. Chabrier), and the true mass of the galaxy, M^*_{dyn}, corrected for the DM contribution. M^*_{dyn}/M^* is found to increase with velocity dispersion, both in low- and high-redshift samples (e.g. Cappellari et al. 2012; Ferreras et al. 2013; Tortora, Romanowsky & Napolitano 2013; Gargiulo et al. 2015). We find that M_{dyn}/M^* varies with velocity dispersion also for cluster spheroids at $z \sim 1.3$, as shown in Fig. 9. We note that the variation holds both for low-density and high-density galaxies, in agreement with what previously found by Gargiulo et al. (2015) for field spheroids at high redshift. For comparison, the M_{dyn}/M^*–σ relation of a sample of local spheroids extracted from the SPIDER sample (grey symbols; La Barbera et al. 2010a) is also shown. We notice that the relation between M_{dyn} and M^*_{dyn}, as well the trend of M^*_{dyn}/M^*–σ, i.e. the variation of IMF on σ and its possible evolution is out of the scope of this work and it is treated in detail in other papers (e.g. Cappellari et al. 2012,
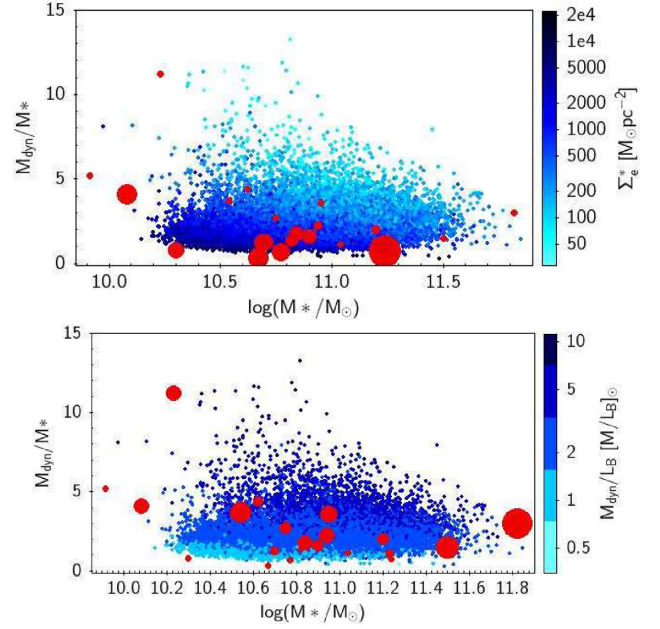
Figure 10. Dynamical to stellar mass ratio as a function of stellar mass for the SPIDER sample (blue dots) and high-redshift cluster spheroids (red dots). The SPIDER galaxies are coded according to their stellar mass density (upper panel) and M_{dyn}/L_B ratio (lower panel). The size of the symbols of high-redshift spheroids (red dots) scales according to their Σ^* and M_{dyn}/L_B.

2013; Ferreras et al. 2013; Tortora et al. 2013; Gargiulo et al. 2015; La Barbera, Ferreras & Vazdekis 2015; Lyubenova et al. 2016; and references therein).

Assuming a Salpeter IMF for low-density spheroids, while keeping the Chabrier IMF for high-density ones, would not change the trend of M_{dyn}/M^* with mass while the offset between $\langle M_{dyn}/M^* \rangle$ values of high- and low-density spheroids (a factor of $\sim$3, see above) would reduce by a factor of 1.7 (e.g. Longhetti & Saracco 2009), remaining still higher for low-density galaxies. As to the formation redshift, the effect of assuming an heavier IMF is that to decrease the z_f derived from the observed $\Delta \log(M_{dyn}/L_B)$, as shown by the green curves in Fig. 7 obtained for $z_f = 6$ with a Salpeter IMF (dashed curve, slope $s = 2.35$) and a significantly bottom-heavy IMF with slope $s = 3.5$ (dot–dashed curve) (see also fig. 10 in Renzini 2006). The right-hand panel of Fig. 8 shows explicitly that, for a given M^*/L_B, lower density spheroids have higher M_{dyn}/L_B and vice versa.

These trends are independent of redshift and of the environment, as shown by Fig. 10 that shows the same quantities of Fig. 8 for a sample of local ($z \sim 0.07$) spheroids. They have been selected from the SPIDER sample (La Barbera et al. 2010a) with $\sigma_e > 150$ km s^{-1} (the range where 17 out of our 22 spheroids lie) and ages older than 7 Gyr, to account for the progenitor bias.[3] The SPIDER galaxies are coded according to their stellar mass density Σ^* (upper panel) and to their M_{dyn}/L_B (lower panel). High-redshift spheroids (red filled points) are superimposed to the local spheroids and the size of their symbols scale according to their Σ^* and M_{dyn}/L_B.

---

[3]We allowed for an age younger than the lookback time $t_{LB} \sim 8.5$ Gyr to account for the progenitor bias, yet leaving room to spheroids that may have experienced a secondary minor burst of star formation at later times. SPIDER sample includes principally spheroidal galaxies in the field and in groups.
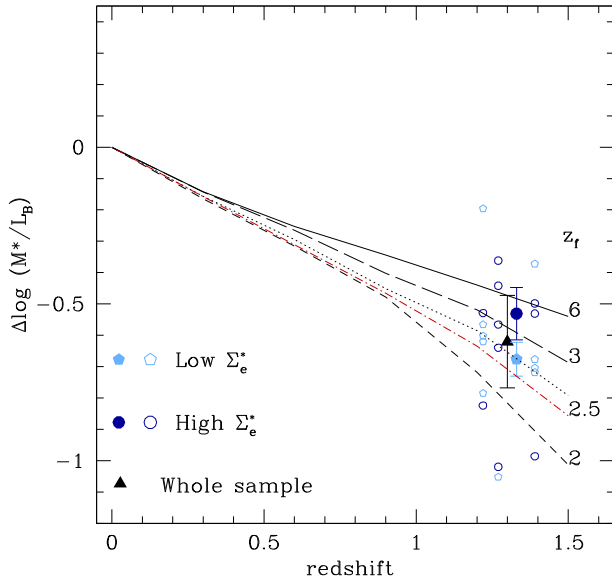
Figure 11. Offset $\Delta\log(M*/L_B)$ for the high-redshift spheroids coded by stellar mass density Σ_e^*. It has been obtained by summing to the $\Delta\log(M_{\rm dyn}/L_B)$ of high-density and low-density galaxies, referred to the median $\log(M_{\rm dyn}/L_B)$ value of local galaxies (like the models), the median $\log(M_{\rm dyn}/M^*) = \log(M_{\rm dyn}/L_B)–\log(M*/L_B)$ computed for high-density and low-density galaxies. Filled black triangle is the median value $\Delta\log(M^*/L_B) \simeq -0.6 \pm 0.1$ of the high-redshift sample. Coloured filled symbols (offset by 0.03 in z for clarity) are the median $\Delta\log$ values of the two subsamples. The curves are as in Fig. 7.

Therefore, $M_{\rm dyn}/M^*$ varies systematically both with stellar mass and mass density, as shown in Figs 8 and 10. In Fig. 11, we compare the observed $\Delta\log(M^*/L_B)$ values of high-density and low-density spheroids to those predicted by SSPs: high-density spheroids experience their last major burst of star formation earlier ($z_{\rm f} \sim 4.5$) than low-density spheroids ($z_{\rm f} < 2.5$), in agreement to the rather well-established evidence that denser galaxies host older stellar populations (e.g. Gargiulo et al. 2009, 2017; Saracco, Longhetti & Andreon 2009; Valentinuzzi et al. 2010; Saracco et al. 2011; Poggianti et al. 2013b; Fagioli et al. 2016; Williams et al. 2017; Díaz-García et al. 2019). Therefore, the formation redshift of cluster spheroids depends on their (dynamical/stellar) mass and it is correlated to the stellar mass density.

6 THE EVOLUTION OF CLUSTER SPHEROIDS

The different slope of the $M_{\rm dyn}/L_B$–$M_{\rm dyn}$ relation at low and high redshift (Fig. 6) implies that $M_{\rm dyn}/L_B$ has varied over time in a different way for low-mass and high-mass galaxies according to equation (7), at least since $z \sim 1.4$. Fig. 7 shows that the variation of $\log(M^*/L_B)$ (skeletal symbol) is consistent with the observed variation of $\log(M_{\rm dyn}/L_B)$ for high-mass galaxies, while it is not sufficient to account for the variation of low-mass galaxies. Assuming that high- and low-mass galaxies have the same stellar IMF, the evolution of the stellar populations account for ~85 per cent of the observed evolution of $M_{\rm dyn}/L_B$ for $M_{\rm dyn} < 10^{11}$ M$_\odot$ spheroids and, hence, that 15($\pm$8) per cent of this evolution must be due to other causes. It is worth to mention that an heavier IMF for low-mass galaxies, like Salpeter IMF, would not account for the different behaviour of $\Delta\log(M_{\rm dyn}/L_B)$ versus $\Delta\log(M^*/L_B)$ (see Fig. 7). Moreover, low-mass galaxies would be expected to have a lighter IMF than high-mass systems. Two other components may affect the evolution of
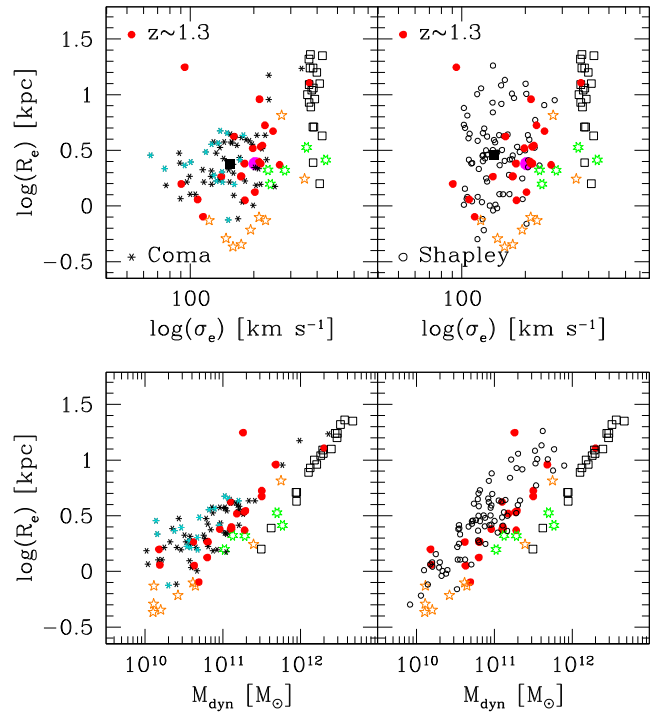
Figure 12. Upper panel: Effective radius versus velocity dispersion relation of high-redshift spheroids (red filled symbols) compared to the relation for the Coma cluster sample (skeletal symbols, left) and the Shapley sample (open circles, right). Cyan skeletal symbols are galaxies younger than 7 Gyr in the Coma cluster (see Section 4.3). The large magenta point is the median value of the high-redshift sample, the large filled square is the median value of the local samples. The open squares are the 23 local massive (0.3–5×10^{12} M$_\odot$) early-type galaxies with $\sigma > 350$ km s^{-1} of Bernardi et al. (2006, 2008); the orange stars are the extremely compact galaxies identified by Damjanov et al. (2013) at $z \sim 0.3$; the green stars are the ultramassive dense early-types at $z \sim 1.4$ by Gargiulo et al. (2016). Lower panel: Effective radius versus dynamical mass relation. Symbols are as in the upper panel.

$M_{\rm dyn}/L_B$, DM and galaxies that join the population of spheroids at later times. Trends of $M_{\rm dyn}/M^*$ shown in Figs 8 and 10 suggest that denser galaxies host a lower fraction of DM (affecting $M_{\rm dyn}$) than lower density ones.[4] However, a different fraction of DM does not produce a mass-dependent evolution of $M_{\rm dyn}/L_B$ (equation 7, Fig. 6). To account for such an evolution, the DM fraction should increase with time more in higher density (lower $M_{\rm dyn}$) galaxies than in lower (higher $M_{\rm dyn}$) ones. However, if this were the case, spheroidal galaxies in the local universe should not display the same $M_{\rm dyn}/M^*$ trends of high-redshift spheroids, that is, higher density galaxies should not have $M_{\rm dyn}/M^*$ values lower than low-density ones, contrary to what it is shown in Fig. 10. Moreover, a variation of the DM fraction can be realized through merging, a mechanism largely disfavoured in cluster environment given the large relative velocities of galaxies (e.g. Treu et al. 2003; Harrison et al. 2011). Actually, Figs 2, 12, and 14 do not show evidences in favour of merging for cluster spheroidal galaxies.

---

[4]It is worth to note that the apertures used for spectroscopic observations sample regions $>>2R_e$ for all the galaxies, with the exception of the largest galaxy of each cluster. Hence, the observed difference between dense and less dense galaxies cannot be ascribed to size aperture effects.
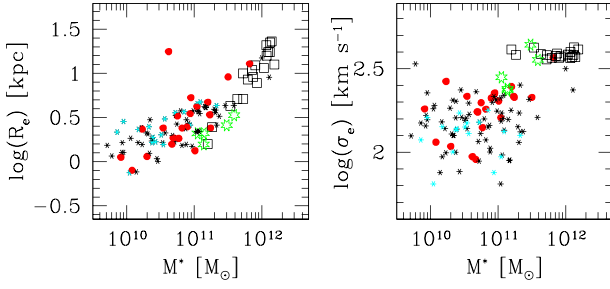
Figure 13. Effective radius (left) and velocity dispersion (right) versus stellar mass for high-redshift and low-redshift (Coma sample) spheroids. Symbols are as in Fig. 12.

Fig. 2 shows that passive aging would bring high-*z* spheroids on to the local Kormendy relation. Hence, structural evolution of individual galaxies is not required and would move them away from the local relation (Jørgensen et al. 2014; Saracco et al. 2014). Fig. 12 shows the effective radius as a function of velocity dispersion (upper panel) and of dynamical mass (lower panel) for high-redshift cluster spheroids (red filled circles) and for the local cluster samples. For comparison, the sample of local BCGs with very large velocity dispersion ($\sigma > 350$ km s^{-1}, open squares) of Bernardi et al. (2008), the sample of extremely compact galaxies identified by Damjanov et al. (2013) (orange stars) at $z \sim 0.3$ and the sample of ultramassive dense early types at $z \sim 1.4$ by Gargiulo et al. (2016) (green starred symbols) are also shown. High-redshift cluster spheroids occupy a region of the σ_e–R_e and M_{dyn}–R_e planes well populated by local cluster spheroids, and all of them have a local counterpart (see also fig. 7 in Beifiori et al. 2017). In case of merging, the region they occupy, especially at small radii and large velocity dispersions and masses (where the most compact/densest galaxies lie), should not be populated by local spheroids, contrary to what happens. This evidence contrasts with the scenario recently proposed by Matharu et al. (2019) in which compact cluster spheroids should disappear over time[5] to justify the observed negligible difference between the mean size of cluster and field spheroids (e.g. Weinmann et al. 2009; Maltby et al. 2010; Cappellari et al. 2013; Fernández Lorenzo et al. 2013; Huertas-Company et al. 2013b; Cebrián & Trujillo 2014; Kelkar et al. 2015; Saracco et al. 2017; Sweet et al. 2017; Mosleh, Tavasoli & Tacchella 2018, but see also Raichoor et al. 2012; Strazzullo et al. 2013; and Andreon 2018 for a different result). It is worth to note that galaxies younger than 7 Gyr in the Coma cluster (cyan symbols, see Section 4.3) are offset with respect to high-redshift galaxies, having preferentially larger R_e and lower σ at fixed mass.

For sake of completeness, in Fig. 13 the effective radius and the velocity dispersion are also shown as a function of stellar mass, relations extensively studied (especially R_e–M^*) in many previous papers of cluster galaxies (e.g. Valentinuzzi et al. 2010; Poggianti et al. 2013b; Jørgensen et al. 2014; Saracco et al. 2014; Andreon, Dong & Raichoor 2017; Beifiori et al. 2017; Saracco et al. 2017; and references therein). The comments on Fig. 12 apply also to Fig. 13.

To admit merging, densest galaxies should be replaced by those that join the population at later times. However, these latter are

---

[5]The disappearance of compact galaxies would be due to merging with the BCG (~40 per cent of them) and to tidal destruction (the remaining 60 per cent). However, merging with BCG would not affect preferentially compact galaxies while tidal forces would destroy preferentially less dense galaxies rather than compact ones.
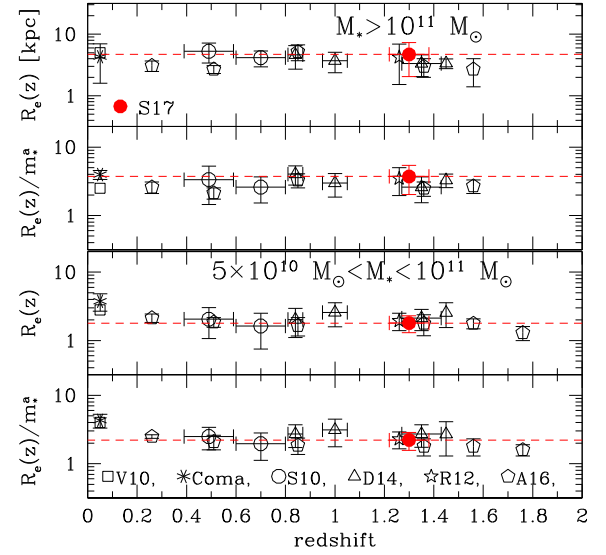
Figure 14. Median size–redshift relation. The median R_e and R_e/m_*^a of cluster early-type galaxies from different samples are shown as a function of redshift in the two ranges of stellar masses $\mathcal{M}_* > 10^{11}$ M$_\odot$ and 5×10^{10} M$_\odot < \mathcal{M}_* < 10^{11}$ M$_\odot$. The different symbols are as follow: filled red circle represents our photometric sample of (55) cluster spheroids at $z \simeq 1.3$ from Saracco et al. (2017, S17); open triangles are the sample of cluster elliptical galaxies (313) at $0.84 < z < 1.45$ by Delaye et al. (2014, D14); open diamonds represent the red-sequence early types (158) in clusters at $0.2 < z < 1.8$ selected by Andreon, Dong & Raichoor (2016, A14); the open star is the sample of cluster and group ellipticals (41) selected at $z \sim 1.27$ by Raichoor et al. (2012, R12); the open circles are the cluster elliptical galaxies (188) at $0.4 < z < 0.8$ studied by Saglia et al. (2010, S10); the starred symbol is the Coma cluster sample, the open square is the median size of local ellipticals from Valentinuzzi et al. (2010, V10; see also Poggianti et al. 2013a). The dashed red line represents the median value of our sample at $z \sim 1.3$.

expected, on average, less dense than those assembled earlier because of the lower density of the universe and the lower star formation rate density. Therefore, they will preferentially have larger radii and relatively lower velocity dispersions (and probably a higher DM fraction within R_e). This agrees with the lack of high-redshift spheroids with low-velocity dispersion (~100–150 km s^{-1}) and large radii ($R_e > 1.5$ kpc) with respect to local ones in Fig. 12.

In Fig. 14, the median effective radius R_e and mass-normalized radius R_e/m_*^a as a function of redshift are shown for different samples of cluster spheroids and for two ranges of stellar masses. Besides our data (red filled point), we plot data from the literature, as reported in the caption of the figure and described in the Appendix. We considered 5×10^{10} M$_\odot$ as lower limit to keep the comparison safe from the different mass limits of the samples. The mass-normalized radius R_e/m_*^a (see e.g. Cimatti, Nipoti & Cassata 2012; Newman et al. 2012; Huertas-Company et al. 2013a; Delaye et al. 2014; Allen et al. 2015; Saracco et al. 2017), where $m_* = \mathcal{M}_*/10^{11}$ and $a = 0.5$ is the slope of the size–mass relation at $z \sim 1.3$ (Saracco et al. 2017), removes the correlation between radius and mass. Fig. 14 does not show evidence of evolution of the median R_e since $z \sim 1.5$ for masses larger than 10^{11} M$_\odot$. Considering the scatter of the data, an increase up to ~40 per cent of the median value of R_e could be present for galaxies with masses $M^* < 10^{11}$ M$_\odot$ at redshift $z < 0.6$ while the data do not show significant variation over the redshift range $0.5 < z < 1.5$ (see also Stott et al. 2011; Huertas-

Company et al. 2013a; Jørgensen et al. 2014; Saracco et al. 2014 for negligible or null size evolution of cluster spheroids).

Thus, the data do not support merging and, hence, a mass-dependent DM variation. On the contrary, the results shown by Figs 12–14 support the scenario in which the spheroids joining the population at later times account for the missing fraction of evolution of M_{dyn}/L_B of the population of spheroids at masses $M_{dyn} < 10^{11}$ M$_\odot$. Concluding, we find evidences that the observed evolution of the FP is mainly due to the evolution of the stellar populations and that galaxies that join the population of spheroids at later times may contribute at masses $<10^{11}$ M$_\odot$ for about 15 per cent of the observed evolution.

7 SUMMARY AND CONCLUSIONS

We obtained LBT-MODS spectroscopic observations for 22 galaxies in the field of the cluster XLSSJ0223−0436 at $z = 1.22$. We confirmed the membership for 12 spheroidal galaxies and determined the stellar velocity dispersion for 7 of them. We combined these data with those in the literature for clusters RXJ0848+4453 at $z = 1.27$ (eight galaxies) and XMMJ2235−2557 at $z = 1.39$ (seven galaxies) to determine the FP of spheroidal galaxies in cluster at $z \sim 1.3$. The analysis related to the FP of high-redshift spheroids and the comparison with that of local cluster spheroids have led to the following results:

(i) The FP of cluster spheroids at $z \sim 1.3$ is offset with respect to the FP of the local comparison samples, the Coma cluster sample and the Shapley sample, and we detect a rotation at $\sim 3\sigma$. The rotation (the different slope) of the FP implies a differential evolution of the population of galaxies along cosmic time. Once expressed as a relation between M_{dyn}/L_B and the total mass M_{dyn}, high-redshift galaxies follow a steeper relation than found for local ones implying a mass-dependent evolution of M_{dyn}/L_B expressed by the relation $\Delta \log(M_{dyn}/L_B) = -0.34\Delta \log(M_{dyn}) + 3.8$.

(ii) Assuming that $\Delta \log(M_{dyn}/L_B) = \Delta \log(M^*/L_B)$, the above relation implies a higher formation redshifts for high-mass galaxies [$z_f \geq 6.5$ for $\log(M_{dyn}/M_\odot) \geq 11.5$] than for low-mass ones [$z_f \leq 2$ for $\log(M_{dyn}/M \leq 10$]. Analogously, we find that galaxies with higher stellar mass density host stellar populations that formed earlier than those in lower mass density galaxies.

(iii) Assuming no variation of the IMF, at fixed stellar mass, lower density spheroids have larger M_{dyn}/M^* and vice versa, suggesting a different DM fraction; the mean M_{dyn}/M^* of low-density spheroids tends to increase for decreasing stellar masses while tends to the constant value of high-density spheroids at large stellar masses. As a consequence of this systematic variation of M_{dyn}/M^*, the observed $\Delta \log(M_{dyn}/L_B)$ for $M_{dyn} > 10^{11}$ M$_\odot$ galaxies is accounted for by the evolution of the stellar populations [$\Delta \log(M^*/L_B)$], while for spheroids with masses $M_{dyn} < 10^{11}$ M$_\odot$ the evolution of M^*/L_B account for ~ 85 per cent of the observed $\Delta \log(M_{dyn}/L_B)$.

(iv) We find no evidence in favour of merging for cluster spheroids of structural evolution of individual galaxies that may produce a differential DM variation to fill in the gap between the evolution of M_{dyn}/L_B and M^*/L_B for lower mass galaxies. On the contrary, we find evidences that spheroids later added to the population may affect the observed $\Delta \log(M_{dyn}/L_B)$ at masses $<10^{11}$ M$_\odot$.

The above findings show that the evolution of the FP of cluster spheroids is consistent with the mass-dependent and mass density-dependent evolution of their stellar populations superimposed to a contribution from spheroids that join the population at later times.

REFERENCES

Allen R. J. et al., 2015, ApJ, 806, 3
Andreon S., 2018, A&A, 617, A53
Andreon S., Dong H., Raichoor A., 2016, A&A, 593, A2
Andreon S., Dong H., Raichoor A., 2017, A&A, 602, C1
Beifiori A., Maraston C., Thomas D., Johansson J., 2011, A&A, 531, A109
Beifiori A. et al., 2017, ApJ, 846, 120
Bernardi M. et al., 2003, AJ, 125, 1866
Bernardi M., Nichol R. C., Sheth R. K., Miller C. J., Brinkmann J., 2006, AJ, 131, 1288
Bernardi M., Hyde J. B., Fritz A., Sheth R. K., Gebhardt K., Nichol R. C., 2008, MNRAS, 391, 1191
Bertin G., Ciotti L., Del Principe M., 2002, A&A, 386, 149
Brooks A., Christensen C., 2016, in Laurikainen E., Peletier R., Gadotti D., eds, Astrophysics and Space Science Library Vol. 418, Galactic Bulges. Springer International Publishing, Switzerland, p. 317
Bruzual G., Charlot S., 2003, MNRAS, 344, 1000
Cappellari M., 2017, MNRAS, 466, 798
Cappellari M., Emsellem E., 2004, PASP, 116, 138
Cappellari M. et al., 2006, MNRAS, 366, 1126
Cappellari M. et al., 2012, Nature, 484, 485
Cappellari M. et al., 2013, MNRAS, 432, 1862
Carollo C. M. et al., 2013, ApJ, 773, 112
Cebrián M., Trujillo I., 2014, MNRAS, 444, 682
Chabrier G., 2003, PASP, 115, 763
Chan J. C. C. et al., 2016, MNRAS, 458, 3181
Cimatti A., Nipoti C., Cassata P., 2012, MNRAS, 422, L62
Ciocca F., Saracco P., Gargiulo A., De Propris R., 2017, MNRAS, 466, 4492
Ciotti L., Lanzoni B., Volonteri M., 2007, ApJ, 658, 65
Damjanov I., Chilingarian I., Hwang H. S., Geller M. J., 2013, ApJ, 775, L48
De Masi C., Vincenzo F., Matteucci F., Rosani G., La Barbera F., Pasquali A., Spitoni E., 2019, MNRAS, 483, 2217
Delaye L. et al., 2014, MNRAS, 441, 203
di Serego Alighieri S. et al., 2005, A&A, 442, 125
Díaz-García L. A. et al., 2019, A&A, 631, 158
Djorgovski S., Davis M., 1987, ApJ, 313, 59
Dressler A., 1980, ApJ, 236, 351
Dressler A., Lynden-Bell D., Burstein D., Davies R. L., Faber S. M., Terlevich R., Wegner G., 1987, ApJ, 313, 42
Fagioli M., Carollo C. M., Renzini A., Lilly S. J., Onodera M., Tacchella S., 2016, ApJ, 831, 173
Fernández Lorenzo M., Sulentic J., Verdes-Montenegro L., Argudo-Fernández M., 2013, MNRAS, 434, 325
Ferreras I., La Barbera F., de la Rosa I. G., Vazdekis A., de Carvalho R. R., Falcón-Barroso J., Ricciardelli E., 2013, MNRAS, 429, L15
Fukugita M., Shimasaku K., Ichikawa T., 1995, PASP, 107, 945
Fukugita M., Hogan C. J., Peebles P. J. E., 1998, ApJ, 503, 518
Gallazzi A., Charlot S., Brinchmann J., White S. D. M., Tremonti C. A., 2005, MNRAS, 362, 41
Gallazzi A., Bell E. F., Zibetti S., Brinchmann J., Kelson D. D., 2014, ApJ, 788, 72

Gargiulo A. et al., 2009, MNRAS, 397, 75

Gargiulo A., Saracco P., Longhetti M., Tamburri S., Lonoce I., Ciocca F., 2015, A&A, 573, A110

Gargiulo A., Saracco P., Tamburri S., Lonoce I., Ciocca F., 2016, A&A, 592, A132

Gargiulo A. et al., 2017, A&A, 606, A113

Glazebrook K. et al., 2017, Nature, 544, 71

Harrison C. D., Colless M., Kuntschner H., Couch W. J., De Propris R., Pracy M. B., 2010, MNRAS, 409, 1455

Harrison C. D., Colless M., Kuntschner H., Couch W. J., de Propris R., Pracy M. B., 2011, MNRAS, 413, 1036

Holden B. P. et al., 2007, ApJ, 670, 190

Holden B. P., van der Wel A., Kelson D. D., Franx M., Illingworth G. D., 2010, ApJ, 724, 714

Huertas-Company M. et al., 2013a, MNRAS, 428, 1715

Huertas-Company M., Shankar F., Mei S., Bernardi M., Aguerri J. A. L., Meert A., Vikram V., 2013b, ApJ, 779, 29

Jørgensen I., 1999, MNRAS, 306, 607

Jørgensen I., Chiboucas K., 2013, AJ, 145, 77

Jørgensen I., Franx M., Kjaergaard P., 1995a, MNRAS, 273, 1097

Jørgensen I., Franx M., Kjaergaard P., 1995b, MNRAS, 276, 1341

Jørgensen I., Franx M., Kjaergaard P., 1996, MNRAS, 280, 167

Jørgensen I., Chiboucas K., Flint K., Bergmann M., Barr J., Davies R., 2006, ApJ, 639, L9

Jørgensen I., Chiboucas K., Toft S., Bergmann M., Zirm A., Schiavon R. P., Grützbauch R., 2014, AJ, 148, 117

Jørgensen I., Chiboucas K., Berkson E., Smith O., Takamiya M., Villaume A., 2017, AJ, 154, 251

Kelkar K., Aragón-Salamanca A., Gray M. E., Maltby D., Vulcani B., De Lucia G., Poggianti B. M., Zaritsky D., 2015, MNRAS, 450, 1246

Kelly B. C., 2007, ApJ, 665, 1489

Kriek M. et al., 2016, Nature, 540, 248

La Barbera F., de Carvalho R. R., de La Rosa I. G., Lopes P. A. A., Kohl-Moreira J. L., Capelato H. V., 2010a, MNRAS, 408, 1313

La Barbera F., de Carvalho R. R., de La Rosa I. G., Lopes P. A. A., 2010b, MNRAS, 408, 1335

La Barbera F., Ferreras I., Vazdekis A., de la Rosa I. G., de Carvalho R. R., Trevisan M., Falcón-Barroso J., Ricciardelli E., 2013, MNRAS, 433, 3017

La Barbera F., Ferreras I., Vazdekis A., 2015, MNRAS, 449, L137

Lanzoni B., Ciotti L., 2003, A&A, 404, 819

Longhetti M., Saracco P., 2009, MNRAS, 394, 774

Lyubenova M. et al., 2016, MNRAS, 463, 3220

Maltby D. T. et al., 2010, MNRAS, 402, 282

Matharu J. et al., 2019, MNRAS, 484, 595

McDermid R. M. et al., 2015, MNRAS, 448, 3484

Mosleh M., Tavasoli S., Tacchella S., 2018, ApJ, 861, 101

Munari U., Sordo R., Castelli F., Zwitter T., 2005, A&A, 442, 1127

Naab T., Johansson P. H., Ostriker J. P., Efstathiou G., 2007, ApJ, 658, 710

Newman A. B., Ellis R. S., Bundy K., Treu T., 2012, ApJ, 746, 162

Newman A. B., Ellis R. S., Andreon S., Treu T., Raichoor A., Trinchieri G., 2014, ApJ, 788, 51

Oser L., Naab T., Ostriker J. P., Johansson P. H., 2012, ApJ, 744, 63

Pahre M. A., Djorgovski S. G., de Carvalho R. R., 1998, AJ, 116, 1591

Pogge R. W. et al., 2010, SPIE, 7735, 77350A

Poggianti B. M. et al., 2013a, ApJ, 762, 77

Poggianti B. M., Moretti A., Calvi R., D'Onofrio M., Valentinuzzi T., Fritz J., Renzini A., 2013b, ApJ, 777, 125

Porter L. A., Somerville R. S., Primack J. R., Johansson P. H., 2014, MNRAS, 444, 942

Prichard L. J. et al., 2017, ApJ, 850, 203

Raichoor A. et al., 2011, ApJ, 732, 12

Raichoor A. et al., 2012, ApJ, 745, 130

Renzini A., 2006, ARA&A, 44, 141

Saglia R. P., Colless M., Burstein D., Davies R. L., McMahan R. K., Wegner G., 2001, MNRAS, 324, 389

Saglia R. P. et al., 2010, A&A, 524, A6

Saglia R. P. et al., 2016, A&A, 596, C1

Saracco P., Longhetti M., Andreon S., 2009, MNRAS, 392, 718

Saracco P., Longhetti M., Gargiulo A., 2011, MNRAS, 412, 2707

Saracco P. et al., 2014, A&A, 567, A94

Saracco P., Gargiulo A., Ciocca F., Marchesini D., 2017, A&A, 597, A122

Saracco P., La Barbera F., Gargiulo A., Mannucci F., Marchesini D., Nonino M., Ciliegi P., 2019, MNRAS, 484, 2281

Sheth R. K., Bernardi M., 2012, MNRAS, 422, 1825

Stott J. P., Collins C. A., Burke C., Hamilton-Morris V., Smith G. P., 2011, MNRAS, 414, 445

Strazzullo V. et al., 2013, ApJ, 772, 118

Sweet S. M. et al., 2017, MNRAS, 464, 2910

Tacchella S., Carollo C. M., Faber S. M., Cibinel A., Dekel A., Koo D. C., Renzini A., Woo J., 2017, ApJ, 844, L1

Tamburri S., Saracco P., Longhetti M., Gargiulo A., Lonoce I., Ciocca F., 2014, A&A, 570, A102

Thomas D., Maraston C., Bender R., Mendes de Oliveira C., 2005, ApJ, 621, 673

Thomas D., Maraston C., Schawinski K., Sarzi M., Silk J., 2010, MNRAS, 404, 1775

Tortora C., Romanowsky A. J., Napolitano N. R., 2013, ApJ, 765, 8

Tortorelli L. et al., 2018, MNRAS, 477, 648

Trager S. C., Faber S. M., Worthey G., González J. J., 2000, AJ, 120, 165

Tremaine S. et al., 2002, ApJ, 574, 740

Treu T., Ellis R. S., Kneib J.-P., Dressler A., Smail I., Czoske O., Oemler A., Natarajan P., 2003, ApJ, 591, 53

Treu T., Ellis R. S., Liao T. X., van Dokkum P. G., 2005a, ApJ, 622, L5

Treu T. et al., 2005b, ApJ, 633, 174

Valentinuzzi T. et al., 2010, ApJ, 712, 226

van de Sande J., Kriek M., Franx M., Bezanson R., van Dokkum P. G., 2015, ApJ, 799, 125

van de Sande J. et al., 2018, NatAs, 2, 483

van der Marel R. P., van Dokkum P. G., 2007, ApJ, 668, 756

van der Wel A. et al., 2007, ApJ, 670, 206

van Dokkum P. G., Stanford S. A., 2003, ApJ, 585, 78

van Dokkum P. G., van der Marel R. P., 2007, ApJ, 655, 30

van Dokkum P. G., Stanford S. A., Holden B. P., Eisenhardt P. R., Dickinson M., Elston R., 2001, ApJ, 552, L101

Vazdekis A., Sánchez-Blázquez P., Falcón-Barroso J., Cenarro A. J., Beasley M. A., Cardiel N., Gorgas J., Peletier R. F., 2010, MNRAS, 404, 1639

Weinmann S. M., Kauffmann G., van den Bosch F. C., Pasquali A., McIntosh D. H., Mo H., Yang X., Guo Y., 2009, MNRAS, 394, 1213

Williams C. C. et al., 2017, ApJ, 838, 94

Woodrum C., Jørgensen I., Fisher R. S., Oberhelman L., Demarco R., Contreras T., Bieker J., 2017, ApJ, 847, 20

Zahid H. J., Geller M. J., 2017, ApJ, 841, 32

APPENDIX A: HIGH-REDSHIFT CLUSTER SAMPLE

The high-redshift sample is composed of 22 cluster spheroidal galaxies in the redshift range $1.2 < z < 1.4$, 7 of which belonging to cluster XLSSJ0223 at $z = 1.22$ (this work, Table 2), 8 spheroids to cluster RXJ0848 (LinxW) at $z = 1.27$ (Jørgensen et al. 2014), and 7 spheroids to cluster XMMJ2235 at $z = 1.39$ (Beifiori et al. 2017). The parameters of these galaxies are summarized in Tables A1 and A2, respectively. Photometry and structural parameters of galaxies belonging to the three clusters considered were derived and extensively studied in previous papers by Saracco et al. (2014) for cluster RXJ0848, Ciocca et al. (2017) for cluster XMMJ2235, and Saracco et al. (2017) for cluster XLSS0223. For RXJ0848, we used the measurements from Jørgensen et al. (2014), given the good agreement between

Table A1. Parameters of spheroidal galaxies in cluster RDCS0848.

ID	ID[a]	z	R_e (kpc)	$\log\langle I_e\rangle$ ($L_\odot\,pc^{-2}$)	σ_e (km s^{-1})	$R_{e,Dev}$ (kpc)	$\log\langle I_e\rangle_{Dev}$ ($L_\odot\,pc^{-2}$)	$\sigma_{e,Dev}$ (km s^{-1})	$\log\mathcal{M}_{dyn}$ ($M_\odot$)	$\log\mathcal{M}_*$ ($M_\odot$)
240		1.261	2.3 ± 0.4	3.37 ± 0.05	265 ± 28	1.3	3.76	275	11.3	10.2
1264		1.273	1.6 ± 0.2	3.26 ± 0.05	91 ± 15	1.6	3.24	90	10.3	10.7
1748	606	1.270	1.8 ± 0.3	3.43 ± 0.05	174 ± 26	2.3	3.30	172	10.8	10.7
2111		1.279	17.6 ± 2.6	1.84 ± 0.04	94 ± 26	3.6	2.86	103	11.3	10.6
2735		1.267	1.1 ± 0.2	3.78 ± 0.05	182 ± 25	1.1	3.82	182	10.6	9.9
2943	1160	1.268	1.8 ± 0.3	3.31 ± 0.05	140 ± 25	2.2	3.19	139	10.6	10.8
2989		1.264	1.1 ± 0.2	3.82 ± 0.05	108 ± 22	1.3	3.76	108	10.2	10.3
3090	3	1.278	1.3 ± 0.2	3.95 ± 0.05	203 ± 19	1.8	3.78	199	10.8	11.0

Notes. All the measurements are taken from Jørgensen et al. (2014).
[a] ID from Saracco et al. (2014).

Table A2. Parameters of spheroidal galaxies in cluster XMMJ2235.

ID	ID_C [a]	z [b]	n	R_e (kpc)	$\log\langle I_e\rangle$ ($L_\odot\,pc^{-2}$)	σ_e [b] (km s^{-1})	$R_{e,Dev}$ (kpc)	$\log\langle I_e\rangle_{Dev}$ ($L_\odot\,pc^{-2}$)	$\sigma_{e,Dev}$ [b] (km s^{-1})	$\log\mathcal{M}_{dyn}$ ($M_\odot$)	$\log\mathcal{M}_*$ ($M_\odot$)
352	1782	1.375	3.6 ± 0.2	3.4 ± 0.5	3.32 ± 0.02	216 ± 53	3.5 ± 0.5	3.28 ± 0.02	216 ± 53	11.27	11.23
407	1790	1.385	4.4 ± 0.3	2.4 ± 0.3	3.64 ± 0.06	213 ± 50	2.2 ± 0.3	3.68 ± 0.06	214 ± 50	11.10	11.24
220	1284	1.390	4.3 ± 0.2	2.4 ± 0.3	3.44 ± 0.02	181 ± 50	2.3 ± 0.3	3.48 ± 0.02	181 ± 50	10.96	10.82
36	2054	1.392	4.4 ± 0.3	4.2 ± 0.6	3.12 ± 0.2	161 ± 31	3.7 ± 0.6	3.19 ± 0.2	162 ± 31	11.10	11.04
170	1740	1.395	3.3 ± 0.2	12.8 ± 2.0	2.62 ± 0.1	368 ± 44	19.5 ± 1.9	2.37 ± 0.1	357 ± 44	12.30	11.82
433	2147	1.395	5.3 ± 0.3	5.3 ± 0.8	2.82 ± 0.1	226 ± 47	3.4 ± 0.8	3.12 ± 0.1	232 ± 47	11.51	10.95
637	–	1.397	3.2 ± 0.2	1.9 ± 0.1	3.76 ± 0.04	172 ± 66	2.3 ± 0.1	3.62 ± 0.04	170 ± 66	10.82	10.69

[a] ID from Ciocca et al. (2017). Structural parameters are those of Ciocca et al. (2017).
[b] Redshift and velocity dispersion measurements are taken from Beifiori et al. (2017). Velocity dispersion values are scaled to the proper effective radii according to equation (1).

our (Saracco et al. 2014), and their measurements (see Jørgensen et al. 2014). In Ciocca et al. (2017), extensive simulations are presented in appendix A1 assessing the robustness of the photometry and of structural parameters derived for the galaxies in cluster XMMJ2235. In the same appendix, simulations dedicated to estimate the errors on the above parameters are also described, while Appendix C is dedicated to a comparison with Chan et al. (2016) measurements showing a good agreement with their published measurements (see fig. C2 of Ciocca et al. 2017).

APPENDIX B: BEST-FITTING LINEAR RELATIONS IN CASE OF CORRELATED ERRORS

Given the correlated errors between variables in some of the relations considered, we repeated the fitting using the code `linmix_err` that applies the Bayesian method proposed by Kelly (2007) to linear regression between data with correlated measurement errors. Table B1 summarizes the relations thus obtained. In all the case considered, correlated errors do not affect significantly the resulting relation.

Table B1. Relations obtained adopting the Bayesian approach by Kelly (2007) to account for correlated errors among variables.

Relation	Reference
$\log\langle I_e\rangle = (-1.48 \pm 0.12)\log(R_e) + (3.90 \pm 0.08)$	$z \simeq 1.3$, spectroscopic sample (Section 4.3)
$\log\langle I_e\rangle = (-1.42 \pm 0.09)\log(R_e) + (3.81 \pm 0.05)$	$z \simeq 1.3$, photometric sample (Section 4.3)
$\log\langle I_e\rangle = (-1.26 \pm 0.06)\log(R_e) + (2.99 \pm 0.03)$	$z = 0$ sample (Section 4.3)
$\log(M_{dyn}/L_B) = (0.57 \pm 0.08)\log(M_{dyn}) - (6.2 \pm 0.9)$	$z \simeq 1.3$ sample (equation 5)
$\log(M_{dyn}/L_B) = (0.32 \pm 0.03)\log(M_{dyn}) - (2.8 \pm 0.2)$	$z = 0$ sample (equation 6)
$\Delta\log(M_{dyn}/L_B) = (0.25 \pm 0.09)\log(M_{dyn}) + (3.4 \pm 0.9)$	(equation 7)
$\log(age(z_f)) = (-0.3 \pm 0.1)\log(M_{dyn}) + (4.0 \pm 0.9)$	(equation 8)
$\log(M_{dyn}/L_B) = (2.1 \pm 0.6)\log(\sigma_e) - (4.7 \pm 1.3)$	$z \simeq 1.3$ sample (Fig. 6)
$\log(M_{dyn}/L_B) = (1.1 \pm 0.5)\log(\sigma_e) - (1.6 \pm 0.9)$	$z = 0$ sample (Fig. 6)

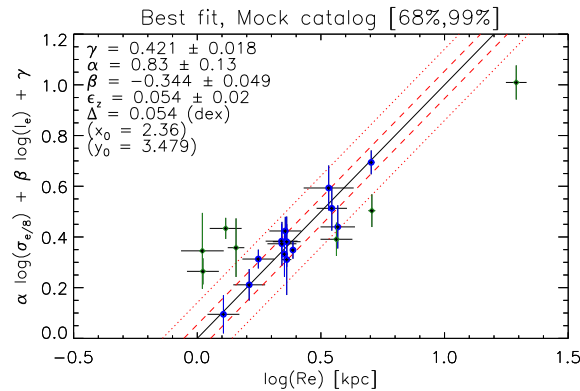## APPENDIX C: BEST-FITTING FP RELATIONS

In this appendix, we show the best-fitting FP relation for the local comparison samples (Fig. C1) and the high-redshift sample (Fig. C2). The best-fitting coefficients α, β, and γ of equation (3) have been determined using the code `lts_planefit` (Cappellari et al. 2013). Note that error bars in the figures should be tilted ellipses rather than crosses due to the correlated errors among variables.
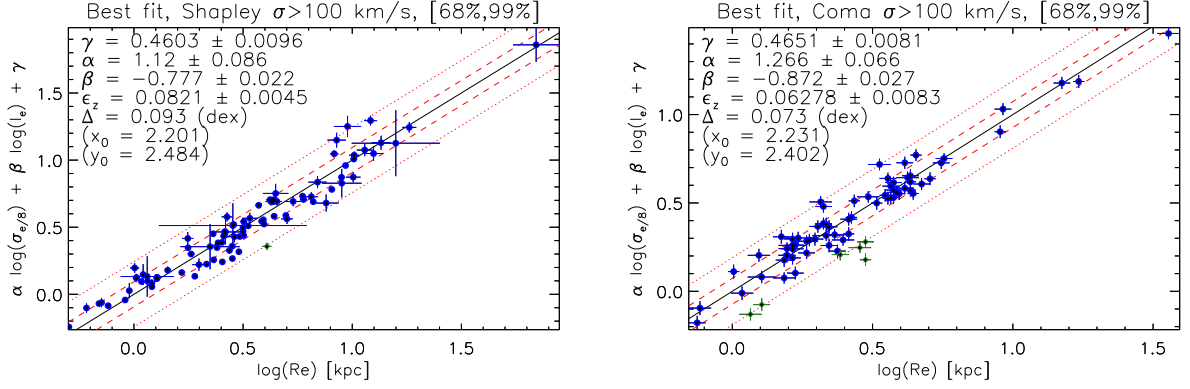
Figure C1. FP of local cluster spheroidal galaxies. The edge-on view of the observed FP and best-fitting relation $\log(R_e) = \alpha \log(\sigma_{e/8}) + \beta \log(I_e) + \gamma$ (equation 3) are shown for the two local samples considered, the Shapley sample (top panel) and the Coma sample (lower panel). The best-fitting values $\alpha \beta \gamma$ are shown at the top left of each panel together with the corresponding observed scatter Δ, the intrinsic scatter ϵ_z, and the pivot values x_0 and y_0 (see Cappellari et al. 2013 for details). The dashed and the dotted (red) lines mark the regions enclosing 68 per cent (1σ) and 99 per cent (2.6σ) of the data, respectively. Green data points are the outliers excluded from the fit by the procedure `lts_planefit`.
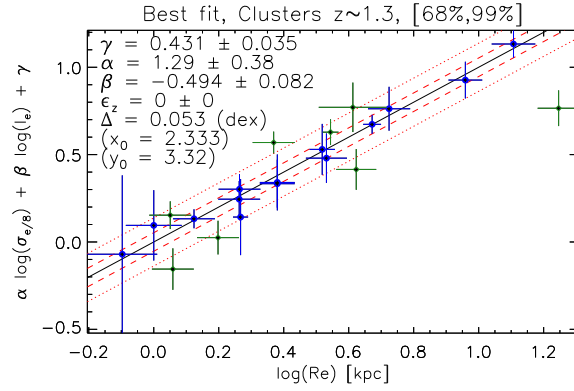
Figure C2. FP of cluster spheroidal galaxies at $z \sim 1.3$. Same as Fig. C1 but for the high-redshift sample composed of the 22 spheroids in cluster at $z \sim 1.3$. Structural parameters are derived from Sérsic profile fitting.

Figure C3. Best-fitting FP obtained for one of the 100 simulated samples of spheroids at $z \sim 1.3$ shown as example. Structural parameters are those derived in case of $r^{1/4}$ profile.

In Fig. C3, the best-fitting FP relation obtained for one of the 100 simulated samples of spheroids at $z \sim 1.3$ is shown as example. Simulated samples consist in varying the values of R_e and L_B of each galaxy by adding a shift δR_e and δL_B randomly chosen from Gaussian distributions with sigmas dR_e and dL_B, respectively, where dR_e and dL_B are the errors on the two parameters. Then, for each galaxy, a new value of I_e is derived from these perturbed values. Structural parameters considered are those obtained with $r^{1/4}$ profile.

APPENDIX D: SIZE–REDSHIFT RELATION DATA

In Fig. 14, besides the sample of 55 spheroids in the three clusters at $z \sim 1.3$ (red filled point; Saracco et al. 2017, S17), the following data samples were considered. The early-type galaxies at $0.4 < z < 0.8$ of the sample of Saglia et al. (2010, S10) based on the ESO Distant Cluster Survey (EDisCS) data set. Stellar masses were derived using a 'diet' Salpeter IMF (see Saglia et al. 2010), resulting similar to a Chabrier IMF. Thus, we did not apply any correction to their masses. On the contrary, according to the recipe of Longhetti & Saracco (2009) (see also Saracco et al. 2014; Tamburri et al. 2014), we scaled by a factor of 1.7 the stellar masses of the early-type galaxies in groups and in cluster at $z \sim 1.27$ selected by Raichoor et al. (2011, 2012, R12), whose masses have been derived using a Salpeter IMF. The same correction has been applied to the sample of red sequence galaxies selected by Andreon et al. (2016, A16) in clusters at $0.2 < z < 1.8$ (see e.g. Tortorelli et al. 2018 for the differences due to different selection criteria). We also plot the cluster early-type galaxies belonging to the sample of Delaye et al. (2014, D14) in the redshift range $0.8 < z < 1.45$ that have stellar masses based on Chabrier IMF, as for our data. All the size measurements are based on *HST*-ACS observations with the exception of measurements at $z > 1$ in the sample of Andreon et al. (2016) based on WFC3 images. For the local Universe, we report the median value of the Coma sample considered in this work (Jørgensen et al. 1995b, starred symbol) and the median value of cluster ellipticals from Valentinuzzi et al. (2010; see also Poggianti et al. 2013a, open square).

This paper has been typeset from a TEX/LATEX file prepared by the author.